

1 **Impact of lateral mixing in the ocean on El Nino in a suite of fully coupled climate models**

2 Anand Gnanadesikan¹, Alexandria Russell¹, Marie-Aude Pradal¹ and Ryan Abernathey²

3

4 1: Department of Earth and Planetary Sciences, Johns Hopkins University, Baltimore, MD USA

5 2: Department of Earth and Environmental Sciences, Columbia University, New York, NY, USA

6

7 Corresponding author: Anand Gnanadesikan (gnanades@jhu.edu)

8

9 Address:

10 327 Olin Hall Johns Hopkins University

11 3400 N. Charles St.

12 Baltimore, MD 21218

13

14 **Key points**

- 15 • The amplitude of El Nino in coupled climate models depends on the diffusion coefficient
16 A_{Redi} that governs the lateral mixing of tracers.
- 17 • Although higher values of A_{Redi} directly damp sea surface temperature anomalies, they
18 indirectly produce higher El Nino amplitudes.
- 19 • As diffusion increases, changes in the mean state of atmosphere and ocean result in both
20 systems becoming more sensitive to variability.

21 **Abstract**

22 We examine the dependence of the amplitude of the El Niño-Southern Oscillation (ENSO) on
23 the mixing coefficient parameterizing the lateral mixing of tracers (A_{Redi}). The value of this
24 coefficient is very uncertain, ranging in Earth System Models between a few hundred and a
25 few thousand m^2s^{-1} , with some observational estimates showing even higher values. A suite of
26 simulations is made with two spatially varying distributions of A_{Redi} derived from satellite
27 observations as well as four simulations where a spatially constant A_{Redi} is varied over a factor of
28 six. Surprisingly, larger values of A_{Redi} result in stronger ENSO variability despite the higher
29 mixing coefficients producing more efficient lateral diffusive damping of anomalies. This is
30 because lateral mixing also warms the cold tongue, increasing vertical temperature gradients and
31 decreasing horizontal temperature gradients. Larger vertical temperature gradients make sea
32 surface temperatures more responsive to atmospheric forcing, while smaller horizontal
33 temperature gradients shift the location of convection and make the atmosphere more responsive
34 to sea surface temperature anomalies. The last effect holds across simulations as well as within
35 individual simulations and thus also helps to explain interdecadal variability in ENSO amplitude.
36 By contrast, a previously proposed anticorrelation between the amplitude interannual and annual
37 variability does not hold across simulations, although it does hold within simulations. The
38 propagation of thermocline depth anomalies is relatively insensitive to the value of A_{Redi} .
39 Properly specifying the lateral mixing along the equator (including distinguishing the impacts of
40 subgridscale turbulence and tropical instability waves) appears essential to simulating ENSO.

41

42

43 1. Introduction

44 The periodic warming and cooling of the tropical Pacific known as the El Niño-Southern
45 Oscillation (ENSO) is a key mode of variability in Earth’s climate, driving changes in
46 temperature and rainfall around the globe. As a result, simulation of ENSO is an important
47 metric for the coupled ocean-atmosphere models used to simulate anthropogenic climate change
48 [Flato *et al.*, 2013]. While the current generation of models performs better than those used in
49 the Coupled Model Intercomparison Project (CMIP) v3 [Kim and Yu, 2012, Bellenger *et al.*,
50 2014], there is still a significant range in the amplitude of sea surface temperature (SST)
51 interannual variability, with different models showing the standard deviation of interannually
52 varying NINO3 (150°W-90°W, 5°S-5°N) SST to range between about 0.5 and 1.4°C. Many of
53 the systematic biases in ENSO simulation have remained unchanged between the CMIP3 and
54 CMIP5 model ensembles [Bellenger *et al.*, 2014]. It is also the case that the amplitude of ENSO
55 changes over time in both observations [Sandweiss *et al.*, 1996,2001; Torrence and Webster,
56 1999; Cobb *et al.*, 2013] and models [Wittenberg, 2006; Stevenson, 2012; Russell and
57 Gnanadesikan, 2014]. Multiple subgridscale parameterizations have the potential to play a role
58 in setting this amplitude, ranging from those associated with cumulus momentum transport [Kim
59 *et al.*, 2007, Neale *et al.* 2008] to the absorption of shortwave radiation in the ocean [Anderson *et*
60 *al.*, 2009]. This paper examines the role of a parameterization that is particularly poorly
61 constrained, namely the lateral mixing of tracers within the ocean.

62 One of the key parameters governing lateral turbulent mixing is the mixing coefficient
63 A_{Redi} , which produces a lateral flux of a tracer C (F_C) such that $F_C = -A_{Redi} \nabla_h C$, where the
64 lateral gradient ∇_h is taken along isopycnal surfaces (following Redi, 1982) in the ocean interior
65 and in the horizontal within the mixed layer. There is considerable uncertainty about how to

66 specify this coefficient. High-resolution simulations that would explicitly represent the mixing
67 process are too expensive for many of the problems to which Earth System Models are applied
68 (carbon cycling, paleoclimate simulations), which require long spinups and production runs.
69 Moreover, even models with extremely high resolution (0.05°) show systematic differences with
70 observational estimates of tracer diffusion, suggesting that they do not capture all the important
71 physics [Tulloch *et al.*, 2014].

72 In the absence of the ability to simulate eddy mixing directly, climate models tend to
73 adopt one of three strategies for choosing a value of A_{Redi} . The first is to simply choose a
74 constant value- as in the HadGEM ($500 \text{ m}^2\text{s}^{-1}$, Jones *et al.*, 2011), GFDL ESM2M ($600 \text{ m}^2\text{s}^{-1}$,
75 Dunne *et al.*, 2012) and INGV CMCC ($2000 \text{ m}^2\text{s}^{-1}$, Fogli *et al.*, 2009). An alternative is to allow
76 the coefficient to vary with grid spacing as in the MPI model (with maximum values of $400 \text{ m}^2\text{s}^{-1}$).
77 A final approach is to draw on the theory for specifying the vertical momentum flux
78 associated with baroclinic instability [Green, 1970; Visbeck *et al.*, 1997], which is used to
79 specify the “thickness” diffusion coefficient A_{GM} [Gent and McWilliams, 1990] which
80 determines the rate at which isopycnals are flattened and to set this equal to A_{Redi} . A_{Redi} has units
81 of length squared times frequency and these theories specify that the frequency is proportional to
82 the baroclinic growth rate. This growth rate is approximated as proportional to the isopycnal
83 slope. If the associated length scales are scaled to the width of the baroclinic zone the result is to
84 produce distributions with high values where isopycnal slopes are steep (e.g. in boundary
85 currents) and low values where isopycnals are flat. This means that values in the tropics in such
86 models are very low indeed. An example of such a distribution for the ESM2Mc model used in
87 this paper is shown in Fig. 1a. Other models that use versions of this representation include the
88 GFDL ESM2G [Dunne *et al.*, 2012] and NorESM [Bentssen *et al.*, 2013]. In both of these models

89 A_{Redi} is independent of depth. In the NCAR CESM model, by contrast [Danabasoglu *et al.*,
90 2012], the length scale increases as the local stratification increases and as the Coriolis
91 frequency decreases. This in turn produces much higher values of A_{Redi} and A_{GM} in the upper
92 200 m (Fig. 1b) as length scales are much larger near the surface, particularly in equatorial
93 regions. Away from the surface, the stratification varies much less with latitude so that the
94 spatial distribution of A_{Redi} and A_{GM} at 500 m in CESM is much more similar to Fig.1a. In the
95 deep ocean in CESM both A_{Redi} and A_{GM} are very small [Danabasoglu and Marshall, 2007].

96 In general, the values of A_{Redi} used in the models are smaller than those estimated from
97 observations. For example the float study of Ollitrault *et al.* [2001] shows large values for
98 dispersion in the subtropical gyres, yielding mixing coefficients of up to $1900 \text{ m}^2\text{s}^{-1}$. Tracer
99 release experiments in the same area [Ledwell *et al.*, 1998] yield dispersion estimates with
100 diffusion coefficients reaching $1500 \text{ m}^2\text{s}^{-1}$ in the zonal direction and $800 \text{ m}^2\text{s}^{-1}$ in the meridional
101 direction. However, these dispersion estimates include both the impact of eddies and of large
102 scale shears, which come to dominate dispersion over long time scales. Such shear flows are
103 even more energetic in equatorial regions, leading to questions about whether large diffusion
104 coefficients estimated there (i.e. up to $9000 \text{ m}^2\text{s}^{-1}$ in Bauer *et al.*, 1998 and $12,000 \text{ m}^2\text{s}^{-1}$ in
105 Lumpkin and Flament, 2001) isolate the impact of the eddies they are supposed to parameterize.

106 Recent work by Abernathey and Marshall [2013] estimates diffusion coefficients using
107 satellite altimetry. Geostrophic velocity fields are calculated from the AVISO product and used
108 to advect passive tracers on a $1/10^\circ$ grid with a background diffusion of $50 \text{ m}^2\text{s}^{-1}$. A_{Redi} can then
109 be estimated from the variance of the fine-scale tracer gradients relative to the large-scale tracer
110 gradients following [Osborn and Cox, 1972]. Because lower background diffusion coefficients
111 result in sharper fine-scale tracer gradients, the estimated diffusion turns out to be relatively

112 insensitive to this background value [Shuckburgh *et al.*, 2009]. In contrast to observational
113 estimates based on floats, the mean velocity is exactly known in such models. This means that
114 the diffusion coefficients are not biased high because of unresolved shear flows. It should be
115 noted, however, that the accuracy of such coefficients, particularly in low latitudes, is determined
116 by the accuracy with which the true velocity field is estimated. Moreover the diffusion
117 coefficient thus derived is a value for the near surface layers, a full theory for extending diffusion
118 to depth has yet to be validated.

119 The field of A_{Redi} computed by *Abernathey and Marshall* [2013] is shown in Fig. 1c. It is
120 readily apparent that the diffusion coefficients shown in Fig. 1c are very different from those in
121 Fig. 1a or 1b. A particularly salient feature of this observational estimate (and most others), is
122 strong latitudinal variation. Enhanced horizontal mixing in the tropics ($> 2000 \text{ m}^2\text{s}^{-1}$) compared
123 with higher latitudes is shown clearly in by the zonal average of this field in Fig. 1d. The high
124 mixing is a consequence of both the high kinetic energy and large spatial scales (associated with
125 larger eddy radii) of low-latitude mesoscale variability [*Klocker and Abernathey*, 2014]. The
126 observational estimate includes the mixing effect of tropical instability waves.

127 It has long been recognized that mixing can have an impact on the structure of the
128 equatorial Pacific. *Maes et al.* [1997] examined the impact of changing lateral diffusion
129 coefficient for both momentum and tracers in a regional model of the tropical Pacific. They
130 found large impacts on the magnitude of the Equatorial Undercurrent, though relatively minor
131 changes in SSTs. This was in part because the high mixing case had much more upwelling from
132 below. On the other hand, *Pezzi and Richards* [2003] showed that decreasing subgridscale
133 mixing in a high-resolution ocean-only model actually increased the temperature of the cold
134 tongue, as it allowed for greater development of tropical instability waves. It did so, however, at

135 the cost of unrealistically increasing the speed of the equatorial undercurrent. They argued that
136 increasing subgridscale lateral mixing near the equator would provide a “best fit” to
137 observations. *Richards and Edwards* [2003] proposed that localized inertial instability could
138 account for such a localized increase. *Lengaigne et al.* [2003] found that the details of mixing
139 mattered, namely whether the mixing was oriented along or across density surfaces. While these
140 studies do highlight the potential importance of subgridscale mixing, they also point out the
141 difficulty of capturing its effects properly. Given the wide range of mixing coefficients
142 documented above, we might hope to isolate the impacts of changing lateral mixing across
143 different GCMs by comparing simulations from the CMIP5 archive. Unfortunately, this is also
144 not possible as there are many processes that differ between models.

145 This paper seeks to isolate the impact of the uncertainty in mixing coefficient on ENSO
146 variability using a single climate model code with different values of the lateral mixing
147 coefficient A_{Redi} . Section 2 describes the simulations we use in this study and outlines the
148 methods we use for identifying the effects of changing the mixing coefficient. Section 3
149 describes the impact of changing A_{Redi} on the mean state and variability of the equatorial Pacific.
150 We find that this coefficient does have an important impact on the amplitude of El Nino.
151 Surprisingly, however, higher values of A_{Redi} result in a stronger El Nino, despite the fact that the
152 higher mixing induces stronger diffusive damping of anomalies. Examining atmospheric and
153 oceanic feedbacks we find that both the ocean and atmosphere become more strongly coupled to
154 each other as the mixing coefficient increases. These indirect effects of increasing the mixing
155 largely swamp the direct effects. Section 4 concludes this paper.

156

157 **2. Models and methods**

158 The model used here is the GFDL ESM2Mc model of *Galbraith et al.* [2011], which is
159 essentially an intermediate between the GFDL CM2.1 model [*Gnanadesikan et al.*, 2006] and
160 ESM2M model [*Dunne et al.*, 2012]. The atmosphere and sea ice models are essentially identical
161 in terms of parameterizations used in CM2.1, ESM2M and ESM2Mc, though ESM2Mc's
162 atmosphere is at a coarser resolution ($3.75^\circ \times 3^\circ$) than the flagship GFDL models ($2.5^\circ \times 2^\circ$). The
163 land model in ESM2Mc is identical to that in CM2.1, with values for albedo and stomatal
164 resistance that are set from data rather than evolving according to a model. The ocean physical
165 model is a coarse-resolution version of the implementation of the Modular Ocean Model 4.0
166 code used in ESM2Mc with a nominal resolution of $3^\circ \times 2^\circ$ (though the zonal resolution varies
167 from 3° in the mid-latitudes to $2/3^\circ$ in the equatorial waveguide). The baseline version of the
168 ESM2Mc model uses a A_{Redi} coefficient of $800 \text{ m}^2 \text{ s}^{-1}$, 1/3 higher than the value in ESM2M and
169 CM2.1. As in ESM2M, the absorption of penetrating shortwave radiation into the ocean is
170 determined by a chlorophyll-dependent absorption coefficient following *Manizza et al.* [2005].
171 As chlorophyll in ESM2Mc is predicted using the Biology, Light Iron, Nutrients and Gasses
172 model of *Galbraith et al.* [2010], changes in chlorophyll associated with ENSO can affect the
173 ocean circulation, a feedback not included in CM2.1.

174 The control model was spun up for 1500 years with well-mixed greenhouse gasses and
175 spatially varying aerosols (sulfate, black carbon, organic carbon, sea salt and multiple size
176 classes of dust) which were fixed at their 1860 levels. Solar forcing is also held constant for all
177 the runs. After 1500 years five additional branches were spun off in which the only change was
178 to A_{Redi} ; all six models were run for 1000 years. Four of the models have spatiotemporally
179 constant values of A_{Redi} (400, 800, 1200 and $2400 \text{ m}^2 \text{ s}^{-1}$), and are referred to in terms of this
180 value as AREDI400, AREDI800, AREDI1200 and AREDI2400 respectively. A run was also

181 spun off the control using the two-dimensional distribution of A_{Redi} from *Abernathey and*
 182 *Marshall* [2013] shown in Fig. 1c, and is referred to as ABER2D. This distribution varies from
 183 very low values in the Southern Ocean to very high values (exceeding $10000 \text{ m}^2\text{s}^{-1}$) in the
 184 subtropical gyres. Finally, in order to evaluate whether it is the full 2-dimensional distribution of
 185 A_{Redi} or rather the latitudinal variability that is important, an additional simulation was made with
 186 a zonally-averaged version of A_{Redi} Fig. 1d). This run is referred to as ABERZONAL. Although
 187 simulated sea surface temperatures equilibrate relatively rapidly, only the last 700 years of output
 188 from each experiment were examined in order to avoid spin-up related biases.

189 Our analysis of feedbacks draws heavily on the work of *Van Oldenborgh et al.* [2005],
 190 who evaluated ENSO in a suite of fourteen climate models included in the Fourth Assessment
 191 Report. They evaluated the models mechanistically by looking at the relationship between
 192 anomalous temperature T' , anomalous wind stress τ' and anomalous thermocline depth z'_{20} . A
 193 linear regression based on the equation

$$194 \quad \frac{\partial T'}{\partial t} = \alpha z'_{20} + \beta \tau' - \gamma T' \quad (1)$$

195 was used to find the coefficients α , β and γ . CM2.1 was one of five models that were judged as
 196 having realistic patterns of these three coefficients. In *Russell and Gnanadesikan* [2014], we
 197 repeated this analysis for the control version of our model and found agreement with
 198 observationally constrained results from the Ensemble Coupled Data Analysis (ECDA, *Zhang et*
 199 *al.*, 2007) that is significantly better than that found in some of the models deemed realistic in
 200 *Van Oldenborgh et al.* [2005]. By quantifying individual connections, this technique allows us to
 201 attribute changes in ENSO variance to changes in the oceanic response, as well as identifying

202 potential tradeoffs between excessively strong and excessively weak feedbacks that might give
 203 us the right answer for the wrong reason.

204 However, simply knowing that the sensitivity of the SST to wind stress or thermocline
 205 depth changes does not tell us what physical process mediates such change. As in *Russell and*
 206 *Gnanadesikan*, [2014] we therefore bring to bear temperature tendencies associated with
 207 individual physical processes. In general, ESM2Mc saves out the following tendency terms

$$\begin{aligned}
 \rho_k \delta z_k c_p \left(\frac{\partial T_k}{\partial t} \right)_{total} &= \\
 &= \rho_k \delta z_k c_p \left\{ \left(\frac{\partial T_k}{\partial t} \right)_{advect} + \left(\frac{\partial T_k}{\partial t} \right)_{neutral} + \left(\frac{\partial T_k}{\partial t} \right)_{submeso} + \left(\frac{\partial T_k}{\partial t} \right)_{vdiff} \right. \\
 &\quad \left. + \left(\frac{\partial T_k}{\partial t} \right)_{nonlocalKPP} + \left(\frac{\partial T_k}{\partial t} \right)_{SWpen} \right\} \quad (2)
 \end{aligned}$$

208 where k is an index of the model level, δz_k is the thickness of that level, ρ_k is the density at that
 209 level and the subscripts refer to specific physical processes. The left-hand side refers to the total
 210 heating/cooling, and the tendencies on the right-hand side are respectively due to resolved
 211 advection, neutral diffusion from both the *Gent and McWilliams* [1990] and Redi-diffusion
 212 terms, submesoscale mixing following *Fox-Kemper et al.*, [2008], vertical turbulent diffusion
 213 that depends on the local vertical gradient, mixed layer turbulent transport by large-eddies that
 214 depends on the temperature gradient across the whole mixed layer rather than just the local
 215 gradient (following *Large et al.*, 1994) and a source term from penetrating shortwave radiation.
 216 We can sum these terms in the vertical from the surface to the Nth box to get

$$\begin{aligned}
\sum_{k=1}^N \rho_k c_p \delta z_k \left(\frac{\partial T_k}{\partial t} \right)_{total} &= Q_{total}^H \\
&= Q_{advect}^H + Q_{neutral}^H + Q_{submeso}^H + Q_{vdiff}^H + Q_{nonlocalKPP}^H + Q_{SWpen}^H \quad (3)
\end{aligned}$$

217 where H is the depth at the bottom of level N.

218 Following (3) we will use the notation $J_X = \rho_k c_p \delta z_k \left(\frac{\partial T}{\partial t} \right)_X$ to refer to heating rates associated
219 with process X in $W m^{-3}$ and Q_X to refer to the layer integrated heat flux associated with process

220 X in $W m^{-3}$. We will then define $\left(\frac{\partial T}{\partial t} \right)_X^H = \frac{Q_X^H}{\rho c_p H}$. In a number of the analyses below we will

221 combine the neutral and submesoscale mixing terms into a single “eddy” term $\left(\frac{\partial T}{\partial t} \right)_{eddy}^H =$

222 $\left(\frac{\partial T}{\partial t} \right)_{neutral}^H + \left(\frac{\partial T}{\partial t} \right)_{submeso}^H$. (with analogous formulation for J and Q terms). We note that since

223 A_{GM} is computed interactively it does change as A_{Redi} changes. However, such changes tend to

224 be localized to convective regions far from where we are focusing.

225 Similarly, we combine the vertical diffusion, KPP and penetrating shortwave radiation

226 terms into two terms, $\left(\frac{\partial T}{\partial t} \right)_{vdiff}^H + \left(\frac{\partial T}{\partial t} \right)_{nonlocalKPP}^H + \left(\frac{\partial T}{\partial t} \right)_{SWpen}^H = \left(\frac{\partial T}{\partial t} \right)_{surf}^H + \left(\frac{\partial T}{\partial t} \right)_{vert}^H$.

227 $\left(\frac{\partial T}{\partial t} \right)_{surf}^H$ is the temperature change over depth H due to surface heat flux Q_{surf} . $\left(\frac{\partial T}{\partial t} \right)_{vert}^H$ is the

228 temperature change due to through the upward flux of heat across depth H due to subgridscale

229 transport depending only on variables that vary in the vertical. It is computed by summing the

230 terms on the left-hand side and subtracting the tendency due to surface heat flux. Including the

231 penetrating shortwave absorption in the vertical transport term is important, as otherwise the

232 dominant signal in this term is simply the redistribution of shortwave radiation within the mixed
 233 layer.

234 We apply this budget analysis in two ways. First, we pick a test volume and examine at
 235 the heat budget within that volume, dividing the individual terms into components that are
 236 correlated with the SST anomaly and residual terms that are not correlated with the temperature
 237 anomaly (either because they are out of phase or because they represent random noise)

$$\begin{aligned} \left(\frac{\partial T}{\partial t}\right)_{total}^H &= \left(\frac{\partial T}{\partial t}\right)_{advect}^H + \left(\frac{\partial T}{\partial t}\right)_{eddy}^H + \left(\frac{\partial T}{\partial t}\right)_{surf}^H + \left(\frac{\partial T}{\partial t}\right)_{vert}^H = \lambda_{total}(H)T' + F \\ &= \lambda_{advect}(H)T' + \lambda_{eddy}(H)T' + \lambda_{surf}T' + \lambda_{vert}(H)T' + F \quad (4) \end{aligned}$$

238 where T' denotes the anomalous SST, F denotes the portion of all forcings that is uncorrelated
 239 with the SST anomaly and the regression coefficients λ denote coefficients scaling the flux that
 240 is in phase (and thus is correlated) with the SST anomaly. We compute the $\lambda_{adv,eddy,surf,vert}$ terms
 241 by regressing the advection, eddy and heat flux terms on temperature anomaly separately. This
 242 method isolates positive and negative feedbacks on upper ocean heat content.

243 Conceptually, such an approach is similar to the derivation of the BJ-stability index in *Jin*
 244 *et al.* [2006] and the heat budget analysis of *Capotondi* [2013]. *Jin et al.* [2006] propose that the
 245 growth of ENSO anomalies can be modeled as

$$\frac{\partial T'}{\partial t} = I_{BJ}T' + F(z_{20}) \quad (5)$$

246 They model the growth rate I_{BJ} in terms of advective anomalies and surface heat fluxes.
 247 Assuming that heat is mixed to mixed layer depth H_{ml} , $I_{BJ} \approx (\lambda_{advect}(H_{ml}) + \lambda_{surf}(H_{ml}))$ in
 248 our analysis. *Jin et al.* [2006] theorize that increases in ENSO amplitude should be related to
 249 increases in I_{BJ} then relate the λ_{advect} term to changes in the ocean temperature and velocity

250 structure and air-sea coupling. However, they neglect the mixing terms- which as we
251 demonstrate below can have a major impact on the in-phase response. Moreover, as noted by
252 *Graham et al.* [2014] the components of the BJ-index that correspond to sensitivity to changes
253 in the thermocline depth and advection do not perfectly correspond to the actual changes seen in
254 the term balances-- highlighting the utility of our approach. In *Capotondi* [2013] the mixing
255 terms are computed as the difference between the total ocean heat content tendency and the sum
256 of the surface heat flux and advective tendency. The total impact of mixing is found to be small
257 for most (though not all) regions, but it should be noted that the formulation of mixing is
258 significantly different from ours. In contrast to *Jin et al.* [2006] who focus on relationships at
259 zero lag, *Capotondi* [2013] considers lagged relationships as well, a point to which we will
260 return later. Our method also differs from *Graham et al* [2014] in that we do not limit our
261 analysis to the mixed layer alone, in part because the appropriate diagnostics are not currently
262 available and in part because (as shown below) important changes in heat transport occur below
263 the mixed layer.

264 Additionally, as in *Russell and Gnanadesikan* [2014] we use the individual time tendency
265 terms $\left(\frac{\partial T}{\partial t}\right)_X^H$ to compute α_X^H , β_X^H and γ_X^H coefficients analogously to equation (1). H will either
266 be taken to be 100m (a depth which lies below the zone of active mixing throughout the
267 simulations in the equatorial Pacific and matches the analysis of *Capotondi et al.* [2013]), or in
268 one analysis at 50m to address the question of sensitivity to the choice of the reference depth. In
269 order to be consistent with previous work, we perform the regression using monthly anomalies in
270 each term. Coefficients are calculated at each grid box and then averaged across latitudes. As
271 shown below, coefficients may change signs within the domain, so by performing this analysis
272 we avoid drawing conclusions that are too dependent on the region chosen. Doing the regression

273 separately for the total, eddy, vertical mixing and advective terms enables us to look at the spatial
274 structure of how different terms change, and to isolate which processes may be making the
275 changes in surface temperature more or less sensitive to changes in forcing.

276 The above analyses primarily focus on how SSTs respond to changes in wind and
277 thermocline depth. This response, however, is only one part of the feedback cycle that regulates
278 El Nino. In order to better understand the full feedback loop, we also regress the anomalous wind
279 stress on the NINO3.4 SST

$$280 \quad \tau'_x(x) = \mu(x) * SST_{NINO3.4} \quad (6)$$

281 and the lagged thermocline depth anomaly on the wind stress over the NINO3.4 region.

$$282 \quad z'_{20}(x) = \phi(x, \delta t) \tau'_x{}^{NINO3.4}(t - \delta t) \quad (7)$$

283 We perform this last set of regressions separately for each lag, as we find that doing a
284 simultaneous regression across many possible lags tends to produce results that are ill-
285 conditioned [Russell and Gnanadesikan, 2014].

286

287 **3. Results**

288 3.1: Changes in the mean state

289 As the coefficients for subgridscale lateral mixing increase, annual mean temperatures
290 along the equator (Fig 2a) increase. This increase is much more pronounced in the cold tongue
291 (SST at 110°W is 0.8°C warmer in AREDI2400 than in AREDI400) than in the warm pool (SST
292 between 100 and 140°E increases by only about 0.1°C). The general pattern of SSTs across the
293 models is shifted to the west relative to observations by about 20°, with the coldest waters

294 centered at 110°W in the models rather than at around 90°W in the observations. The
295 temperatures for this preindustrial run are about 1°C lower than modern observations, reflecting
296 in part the lack of radiative forcing from greenhouse gasses. If we focus instead on the
297 temperature difference relative to 150-160°E in the center of the warm pool (Fig. 2b), we see that
298 the models generally underestimate the modern gradient across the basin, with the low mixing
299 runs lying closest to the observations and the high-mixing runs showing the weakest gradient. It
300 should be noted, however, that this result is quite dependent on the latitude range used- when the
301 analysis is done from 3.6°S to 3.6°N (not shown here) the low and high mixing cases bracket
302 observations west of about 140°W. The 20°C isotherm (Fig. 2c) is well simulated in the low
303 mixing runs, and becomes a little shallower than observations in the warm pool in the higher
304 mixing runs. Over the NINO3.4 region, the decrease in isotherm depth from AREDI400 to
305 AREDI2400 is around 7m. The annual mean zonal wind stresses (Fig 2d) reflect the differences
306 in SST, with the magnitude of peak easterly wind stress about 10% lower in AREDI2400 than in
307 AREDI400 and also shifted somewhat westward. The modeled wind stresses lie between the
308 ERA-Interim (black symbols) and ECDA (red symbols) products over much of the western
309 basin, illustrating the difficulty in picking a “best” model. In general the differences between the
310 models and observations are typical of those seen in the CMIP3 and CMIP5 ensembles
311 [Bellenger *et al.*, 2014].

312 The mechanism by which increasing A_{Redi} increases temperatures is shown in Fig. 3. At
313 140°W in the AREDI2400 model, temperature (colors, Fig. 3a) tends to decrease along neutral
314 density surface (horizontal grid lines) as one moves towards the equator. As a result neutral
315 diffusion moves heat upwards into the mixed layer (Fig. 3b), cooling the subsurface and
316 warming the surface. Subsurface cooling rates $J_{neutral}$ are as high as -6 W m^{-3} , sufficient to

317 produce cooling of $-0.12 \text{ }^\circ\text{C day}^{-1}$. Warming rates are smaller in magnitude but cover a larger
318 fraction of the water column. The difference between $J_{neutral}$ in the AREDI2400 and
319 AREDI400 simulations (colors, Fig 3c) looks almost identical to $J_{neutral}$ in AREDI2400
320 illustrating that lateral diffusive heating is negligible in the low mixing simulation. Although the
321 neutral diffusive term includes both contributions from both eddy advection associated with A_{GM}
322 and eddy diffusion associated with A_{Redi} , examination of both the A_{GM} and its associated
323 overturning show minimal (less than 10%) changes as A_{Redi} changes, whereas the pattern of
324 heating largely scales with A_{Redi} (not shown here, but seen when looking at other pairs of
325 simulations). Changes in submesoscale mixing (not shown) are also small, so this pattern also
326 reflects changes seen in J_{eddy} .

327 In order to reach a new steady state, however, this increased upward transport of heat
328 must be balanced by an increased downward transport of heat from some other process. As
329 shown by the contours in Fig. 3c, this process is largely the parameterized small-scale vertical
330 mixing J_{vdiff} . As the surface becomes warmer and the deep ocean cooler as a result of
331 increasing A_{Redi} , vertical mixing acts to transport more heat downward across the increased
332 gradient, eventually establishing a new balance with more cooling (negative J_{vdiff}) near the base
333 of the mixed layer and more heating (positive J_{vdiff}) below that. The increased vertical transport
334 is a function of the increased vertical temperature gradient, as the vertical turbulent diffusive
335 coefficient (not shown) actually decreases in this section throughout the top 150m.

336

337 3.2 Changes in interannual variability

338 Although all the models appear to show a relatively high degree of fidelity to
339 observations when it comes to the mean metrics in Fig. 2, this is not as true for variability. The
340 standard deviation of interannually smoothed SST (Fig 4a) shows that the lower frequency
341 anomalies are much more peaked in the central Pacific than the observed anomalies, which are
342 relatively flat from the dateline to the Galapagos. While the two low-mixing cases (AREDI400
343 and AREDI800) produce a level of SST variability close to the observed values, the higher
344 mixing cases have noticeably higher variability (Fig. 4a,d, Table 1). Looking at these separately
345 in each century gives us estimates of the uncertainty associated with the mean value, which
346 varies between about 3 and 5% of the mean across the different models. This suggests that the
347 differences between AREDI400 and AREDI800 are unlikely to be statistically significant but
348 that the differences between these runs and AREDI1200, AREDI2400, ABER2D and
349 ABERZONAL are. The differences between models are smaller in the Western Pacific, with
350 the curves converging west of the dateline.

351 Annually smoothed wind stress anomalies (Fig. 4b) are even more biased, with large
352 values in the west Pacific not seen in the reanalyses. As mixing increases, models show more
353 interannual variability in the wind stress, particularly over the central Pacific. If we only
354 consider the NINO3.4 latitude band from 170°W to 120°W, the wind stress anomalies are more
355 than 50% larger in ABERZONAL than in AREDI400 (Table 1). Note that within this region the
356 models essentially span the range of the reanalyses.

357 Variability in the depth of the 20°C isotherm has been recently analyzed in terms of two
358 modes, a “tilt” mode which involves a tilting of the thermocline and a “warm water volume”
359 mode involving a deepening of the thermocline [*Capotondi, 2013, Bunge and Clarke, 2014*]. The
360 first of these corresponds to the first EOF of z_{20} variability and would be expected to produce

361 two peaks (with a minimum at the “pivot point” of the tilt) while the second produces more
362 uniform variability. The sum of the two patterns is reflected in the observed z_{20} variability (Fig.
363 4c). The models also produce two peaks with a central valley, but the peaks tend to be too large
364 and are offset from the observed locations. When examining EOFs of the thermocline depth, we
365 found that the models produce a “tilt mode” that is centered further to the east than in
366 the observations. As mixing increases, z_{20} anomalies in the NINO3.4 region change from 6.3m
367 in AREDI400 to 8.7m in ABERZONAL (Table 1), representing an almost twofold change in
368 variance. The higher model variance could be due to stronger forcing of the z_{20} anomalies by
369 unrealistically strong winds or to an overly strong response of the thermocline to winds.

370 Time series illustrate that the overall increase in variance also involves an increase in the
371 long-term variability of that variance. On a 40 year time scale, the models simulate a wide range
372 of variances, with the NINO3.4 variance ranging from $0.35 \text{ }^{\circ}\text{C}^2$ to $1.06 \text{ }^{\circ}\text{C}^2$ in AREDI400 and
373 $0.52 \text{ }^{\circ}\text{C}^2$ to $1.76 \text{ }^{\circ}\text{C}^2$ in ABERZONAL. It is instructive to note the difficulties this raises for
374 validating models with the short observational record. The least active 40-year epoch in the most
375 active model (ABERZONAL) has a variance half that of the most active 40-year epoch in the
376 least active model (AREDI400). As noted in *Russell and Gnanadesikan* [2014] similar temporal
377 variability is found in coupling strengths as well. This variability highlights the necessity for
378 long time series (as previously noted by *Stevenson et al.*, [2010,2012]) to distinguish systematic
379 differences between models from internal variability.

380 In order to determine whether changes in the amplitude of variability are also associated
381 with changes in the frequency of variability we computed wavelet spectra of the variability of
382 NINO3.4 SSTs from the ECDA and Reynolds SST datasets and from the six models using a
383 complex Morlet wavelet. The resulting wavelet spectra (presented normalized by frequency so

384 that results are per octave) are shown in Fig. 5a. The AREDI400 and AREDI800 cases are
385 essentially indistinguishable and show a peak with a relatively realistic amplitude but at
386 somewhat longer periods (4-6 years) than in the observations. All of the higher mixing cases
387 show a substantial increase in the amplitude of this peak which appears in each of the centuries
388 analyzed.

389 Although there is some suggestion from the spectra of a negative relationship between
390 the amplitude of interannual variability and the amplitude of annual variability, as noted in
391 previous work [*Torrence and Webster, 1999, Guilyardi, 2006*] the picture is not simple. For
392 example, AREDI400 and AREDI2400 have very similar near-annual spectral densities, but very
393 different interannual spectral densities. When we plot the variance in the near-annual band
394 (periods of 0.94-1.12 years) vs. the interannual band spanning periods of 1.6-8.2 years (Fig. 5b)
395 a complex picture emerges. Within individual models, particularly those with higher mixing
396 rates, anticorrelation between the amplitudes of annual and interannual variability over 40 yer
397 periods is as high as -0.65 (in the AREDI2400 model). However, within the AREDI400 model
398 the correlation is only -0.34, accounting for about 10% of the variance. Moreover, the slopes that
399 emerge across the different runs are quite different. Not only does the mechanism relating annual
400 and interannual variability appear to work differently in the different model runs, the relationship
401 does not appear to change in a consistent manner as the mixing increases (in contrast, as we will
402 see below, to the mean gradient along the equator).

403

404 3.3: Changes in anomaly development and damping

405 It is surprising that ENSO variability increases as mixing increases, as we would expect
406 more mixing to produce stronger damping of anomalies. To understand this counterintuitive
407 result, we begin by applying equation (4) to the horizontally averaged temperature anomalies in
408 the NINO3.4 band of longitudes between 170°W and 120°W. Because we wish to focus on the
409 center of the anomalies, we focus on the heat budget over the top 100m between 3.6°S and
410 3.6°N. When regression coefficients are calculated over single centuries, we find a variance of
411 about 10% in the mean value, implying that with 7 independent estimates, the true regression
412 coefficients are estimated to within about 3%.

413 We would expect that the regression coefficient $\lambda_{eddy}(100m)$ would become more and
414 more negative as A_{Redi} increases. As shown by the first set of bars in Fig. 6, this is in fact the
415 case, with the coefficient for AREDI400 being $-0.010 \text{ month}^{-1}$ and that for AREDI2400 being
416 $-0.079 \text{ month}^{-1}$. As A_{GM} does not change significantly between the different runs, this rough
417 proportionality also supports our contention that the changes in neutral diffusive tendency are
418 primarily driven by the subgridscale diffusion rather than eddy advection.

419 However, stronger lateral diffusive damping is significantly offset by weaker damping
420 from changes in vertical subgridscale processes. The second set of bars in Fig. 6 shows
421 $\lambda_{vert}(100m)$ which quantifies how mixing of cold water from below correlates with ENSO
422 variability. As noted by *Lengaigne et al.* [2012], during El Ninos the mixing of cold water from
423 below drops, while during La Ninas it rises. This vertical diffusive flux of heat at 100m thus
424 represents a positive feedback on SST anomalies. As A_{Redi} increases the resulting growth rate
425 increases as well, rising from 0.020 month^{-1} in AREDI400 to 0.069 month^{-1} in AREDI2400.
426 Interannual changes in lateral and vertical diffusive fluxes thus tend to balance in our model, just
427 as their long term means do in Fig. 3.

428 Other processes play an important role in the overall balance, but are less sensitive to
429 changes in mixing. The third set of bars in Fig. 6 shows $\lambda_{surf}(100m)$, which characterizes the
430 sensitivity of surface heat fluxes to temperature anomalies. This term tends to damp anomalies,
431 giving more cooling when the SST is high and less cooling when it is colder. $\lambda_{surf}(100m)$ shows
432 a small increase in magnitude from $-0.074 \text{ month}^{-1}$ in AREDI400 to $-0.082 \text{ month}^{-1}$ in
433 AREDI2400, so that the higher mixing case is more strongly damped overall. Similarly, the
434 fourth set of bars shows $\lambda_{advect}(100m)$ which characterizes how strongly the advection of heat
435 reinforces the temperature anomaly. This growth rate strengthens from 0.043 month^{-1} in
436 AREDI400 to 0.059 month^{-1} in AREDI2400, consistent with the increase in wind stress
437 variability seen as the mixing increases. The behavior of the advective and vertical mixing terms
438 is superficially analogous to the “equatorial thermostat” effect proposed by *Clement et al.*
439 [1996], in which a warmer surface is associated with stronger vertical gradients and thus stronger
440 dynamical cooling. In contrast to that work, (where advection of heat plays the primary role) in
441 our model changes in vertical diffusive mixing are much more sensitive to the change in
442 background stratification.

443 When all of the fluxes are added together, (rightmost set of bars in Fig. 6) we see that
444 temperature anomalies in the NINO3.4 region are more strongly damped as the mixing increases.
445 The total damping coefficient increases from $-0.021 \text{ month}^{-1}$ for AREDI400 to $-0.030 \text{ month}^{-1}$
446 for AREDI2400. These changes in damping work in the opposite sense from changes in ENSO
447 variability.

448 The impact of including spatially-dependent mixing is not straightforward. Although
449 ABER2D has maximum A_{Redi} in the gyre interiors exceeding $10000 \text{ m}^2\text{s}^{-1}$, the total damping rate
450 $\lambda_{total}(100m)$ ($-0.029 \text{ month}^{-1}$), eddy damping rate $\lambda_{eddy}(100m)$ ($-0.066 \text{ month}^{-1}$) and vertical flux

451 rate $\lambda_{vert}(100m)$ (0.060 month^{-1}) all lie between those found for AREDI1200 and AREDI2400.
452 However, $\lambda_{eddy}(100m)$ is 1/3 larger in ABERZONAL ($-0.097 \text{ month}^{-1}$) than in AREDI2400. On
453 the other hand, $\lambda_{vert}(100m)$ (0.085 month^{-1}) is so large that it essentially cancels the damping
454 from surface heat fluxes $\lambda_{surf}(100m)$ of $-0.082 \text{ month}^{-1}$. $\lambda_{advect}(100m)$ is slightly smaller than in
455 AREDI2400, with a value of 0.059 month^{-1} . When all terms are added up, the ABERZONAL
456 case has the strongest total damping rate $\lambda_{total}(100m)$ ($-0.0354 \text{ month}^{-1}$) despite having the
457 largest variability.

458 As noted above, the BJ stability analysis isolates the impacts of advection and surface
459 heat fluxes on ENSO. Adding $\lambda_{advect}(100m) + \lambda_{surf}(100m)$ we find that the sum does
460 increase from $-0.031 \text{ month}^{-1}$ in AREDI400 to $-0.023 \text{ month}^{-1}$ in AREDI2400 a 28% decline in
461 damping which is quite consistent with the 21% increase in NINO34 amplitude. Superficially,
462 this supports the use of the analysis of *Jin et al.* [2006] to understand changes in ENSO.
463 However, we note that this apparent agreement is only possible because we ignore changes in the
464 mixing of heat from below and laterally which are even larger in magnitude: the sum of which
465 changes from $+0.010 \text{ month}^{-1}$ for AREDI400 to $-0.007 \text{ month}^{-1}$ for AREDI2400, resulting in the
466 net increase of damping seen in Fig. 6.

467 A strengthening of spatially-averaged damping of anomalies obviously cannot explain the
468 increase in ENSO variance. This means that the forcing term in equation (4) must be considered
469 as well. If this term were only due to white noise, an increase of about 70% in the amplitude of
470 this noise would be required to explain the increase in ENSO in the presence of increased
471 damping. Such a mechanism was invoked by *Manucharyan and Federov* [2014] to explain the
472 decrease in variance in past climates with low along-equator temperature gradients. However,

473 when we examine the amplitude of F (removing the part of $\left(\frac{\partial T}{\partial t}\right)_{total}^H$ that is correlated with T')
474 we find that the amplitude only changes by about 10%. This means that the exact phasing of F
475 matters, making it important to divide variation between more variables as in *van Oldenborgh et*
476 *al.*, [2005] and *Russell and Gnanadesikan* [2014]. Additionally, as previously noted, if increases
477 in damping rates are spatially separated from increases in forcing rates, results from area-
478 averaged regressions may be deceptive.

479 For this reason we now turn to the analysis of *van Oldenborgh et al.* [2005] as given in
480 equation (1), focusing on the forcing of the sea surface temperature anomalies. The thermocline
481 depth response coefficient α (Fig. 7a) shows some changes as the mixing increases, with the
482 ocean becoming more responsive to changes in the thermocline depth. In particular, the “valley”
483 that appears in the response at around 115°W appears to fill in as the mixing increases. Note that
484 this makes the response less like that in ECDA. The wind stress coefficient (Fig. 7b) β shows
485 similar changes, with the ocean becoming more responsive in the eastern basin. An increase in
486 responsiveness is exactly what would be expected from the increase in ENSO amplitude with
487 increasing mixing coefficient. The damping time scale (Fig. 7c, used for ease in comparing our
488 results with *van Oldenborgh et al.*, 2005) $1/\gamma$ shows a more complex picture. There is a shorter
489 damping time scale in the east as the mixing increases, which would tend to decrease ENSO
490 amplitude. In the west, however, the time scale drops as the mixing increases from AREDI400 to
491 AREDI1200, then drops again for AREDI2400. The ABER2D and ABERZONAL models look
492 more like the high-mixing than the low-mixing models, though with somewhat different shapes.
493 The wind stress coefficient β for ABERZONAL is very close to that for AREDI2400, but the
494 thermocline depth coefficient α is higher east of 140°W in ABERZONAL than in any of the

495 other models. The thermocline depth coefficient α in ABER2D is closer to that for AREDI800
496 near 110°W, but is higher than AREDI2400 (and closer to ABERZONAL) at 140°W.

497 As in *Russell and Gnanadesikan* [2014], we extend this regression to look at heat content
498 anomalies at different depths and break it down into different terms due to different physical
499 processes. Fig. 8 shows this decomposition over the top 100m. The columns correspond to the
500 time tendencies associated with different processes and the rows to different coefficients.
501 Because of the different ranges of the various forcing fields, it is not immediately straightforward
502 to compare differences across the different tendency terms while retaining MKS units. We note
503 that a reasonable scale for the thermocline depth changes is $\sim 10\text{m}$, so that the corresponding
504 advective contributions to α from a “typical” increase in z_{20} (Figs. 8a) would range between
505 $+0.12 \text{ K month}^{-1}$ in the central Pacific to $-0.22 \text{ K month}^{-1}$ in the eastern Pacific. The change in
506 sign at around 120°W suggests that one would find a very different response to thermocline
507 depth anomalies in the NINO3 region (150°W-90°W), which has significant compensation
508 between positive and negative regions vs. the NINO3.4 region (170°W-120°W), which is all of
509 the same sign. In the NINO3.4 region a deeper thermocline is associated with advective
510 warming, whereas to the east of this region it is associated with advective cooling. Such a result
511 shows the importance of considering the spatial pattern of responses. Over the top 100m the
512 vertical diffusive contribution (Fig. 8b) and lateral diffusive contribution (Fig. 8c) to the
513 thermocline depth response are much smaller. Note that α_{eddy}^{100m} (though small) is actually
514 positive around 110°W, so that a deep thermocline in this region is associated with more lateral
515 diffusive supply of warm water, possibly because it can be supplied over a wider depth range.

516 For the wind stress parameters the advective response (β_{advect}^{100m} , Fig. 8d) shows a broad
517 positive response in the central Equatorial Pacific, a negative response near about 90°W and a

518 positive response along the Southern American coast. Given anomalies in the last region of order
519 0.003 Pa (Fig. 4b) the resulting warming/cooling of the top 100m is of order 0.1 K month^{-1} . By
520 contrast, the impact of wind stress on 1-D vertical heat fluxes (Fig. 8e) shows a broad peak in the
521 central Pacific somewhat to the west at around 120°W , and given values of wind stress anomaly
522 around 0.004 Pa in this region, the resulting heating is around $0.03 \text{ K month}^{-1}$. Stronger eastward
523 stress appears to be associated with more positive lateral heat flux to the near-equatorial zone
524 (Fig. 8f), particularly in models with higher mixing, for reasons that are currently unclear, though
525 the impact is small.

526 Our expectation that increasing the mixing coefficient would increase the damping rate is
527 borne out in Fig. 8i, which shows a steady increase in the damping rate due to mesoscale and
528 submesoscale eddy processes γ_{eddy}^{100m} across the constant runs. The ABERZONAL simulation ends
529 up producing a damping rate γ_{eddy}^{100m} that lies above the AREDI2400 throughout the basin, while
530 the ABER2D run is higher than all of the others only in a small range of longitudes in the
531 western part of the basin but is close to AREDI2400 in the eastern part of the basin. Again, the
532 different spatial patterns of change demonstrate the importance of not simply building a theory
533 based on a single region.

534 The increased damping from lateral diffusion is significantly balanced, however, by other
535 processes, as in Fig. 6. Fig. 8h shows a decrease in the damping coefficient associated with 1D
536 vertical transport of heat $\gamma_{vert}^{100m} + \gamma_{surf}^{100m}$ as the mixing increases. Again this change shows
537 centers of action around 160°E and 120°W . In the far western Pacific, the impact of mixing on
538 $\gamma_{vert}^{100m} + \gamma_{surf}^{100m}$ actually switches sign for the highest values of A_{Redi} . Advective fluxes (Fig. 8g,
539 γ_{advect}^{100m}) tend to be positively correlated with temperature away from the NINO3.4 region, but

540 damp temperature anomalies to the east and west of this region. As mixing increases the region
541 of large advective impact shifts eastward.

542 Because of the different vertical scales in Fig. 8, it is challenging to visualize the impact
543 of changing A_{Redi} on the different coefficients. Thus in Fig. 9 we examine the difference between
544 ABERZONAL (the model with the strongest ENSO) and AREDI400 (the model with the
545 weakest ENSO) across the α, β and γ coefficients. We do this for two integration depths. A depth
546 $H=100$ m (left-hand column) corresponds to our analysis in Figs. 6 and 8 and is also a reasonable
547 depth to look at changes in warm water volume that would reflect the recharge-discharge
548 oscillator theory. We also look at $H=50$ m (right-hand column), so as to examine how changes in
549 heat content at depth propagate up to the surface. $\gamma_{\text{eddy}}^{100m}$ (black line, Fig. 9e) increases by up to
550 more than 0.1 month^{-1} near the date line, so that a larger mixing coefficient does indeed result in
551 stronger diffusive damping of anomalies. As before, however, the change in $\gamma_{\text{vert}}^{100m} + \gamma_{\text{surf}}^{100m}$
552 (blue line, Fig. 9e), largely cancels the additional damping associated with lateral diffusion.
553 Additionally, $\gamma_{\text{advect}}^{100m}$ (which is generally negative, indicating a positive feedback on
554 temperature) becomes more negative in the central basin as the mixing increases (red line Fig.
555 9e). A small positive peak in $\gamma_{\text{advect}}^{100m}$ shifts east as the mixing increases. Because the eddy and
556 vertical diffusive components largely balance each other, it is this change in the advective
557 component that largely accounts for the decrease in damping in the western basin and increase in
558 the eastern basin in Fig. 7c. This is also the case when a shallower integration (Fig. 9f) is taken.

559 Advection also plays a dominant role in explaining the increase of thermocline depth
560 sensitivity α as A_{Redi} increases. When the integration is taken over the top 100m (Fig. 9a), $\alpha_{\text{eddy}}^{100m}$
561 and $\alpha_{\text{vert}}^{100m} + \alpha_{\text{surf}}^{100m}$ largely cancel while $\alpha_{\text{advect}}^{100m}$ increases in the eastern basin. The result would

562 be to decrease sensitivity to z_{20} in the central basin, and increase it in the eastern basin. When
563 the integration is taken over the top 50m (Fig. 9b) the cancellation between $\alpha_{vert}^{50m} + \alpha_{surf}^{50m}$ and
564 α_{eddy}^{50m} is more exact and the sign of the advection term α_{advect}^{50m} is positive over a wider range,
565 more consistent with the surface SST regression in Fig. 7a.

566 The western decline and eastern increase of the wind stress response coefficient β seen in
567 Fig 7b can also largely be attributed to advective processes (Fig. 8d,9c). As stratification
568 increases, the advective cooling of the surface becomes more responsive to anomalous wind
569 stress and $\beta_{advect}^{50m,100m}$ increase. Vertical diffusive processes reduce the response to anomalous
570 winds across the basin. This enhances the suppression of the wind stress response in the western
571 basin, while countering its increase slightly in the eastern basin. Note that again there is
572 somewhat of a disconnect between the behavior at 100m and that at 50m (Fig. 9d) with the eddy
573 and vertical diffusive transport over the shallower depth range showing much less sensitivity to
574 winds, while advection shows the same increase in the eastern basin and decrease in the central
575 basin seen in the analysis of SSTs in Fig. 7b.

576 While the increase in the responsiveness of the eastern Pacific to wind and temperature
577 anomalies under higher mixing is consistent with the increase of temperature variance, the
578 response of the SST represents only one part of the feedback loops setting up ENSO. We now
579 examine the role of the rest of the loop, beginning with the coefficients $\mu(x)$ linking wind stress
580 to NINO3.4 anomalies (Fig. 10a). As mixing increases, the basic state of the atmosphere is
581 more responsive in the cases with higher mixing in the central Pacific, and less responsive in the
582 western Pacific. If we compute the Bjerknes feedback parameter $\bar{\mu}$ by regressing NINO4 wind
583 stress against NINO3 SSTs as in *Bellenger et al.* [2014], the parameter ranges from 10.4×10^{-3} N

584 $^{\circ}\text{C}^{-1}$ in AREDI400 to $11.3 \times 10^{-3} \text{ N } ^{\circ}\text{C}^{-1}$ in ABERZONAL. While these values are relatively
585 close to the $12 \times 10^{-3} \text{ N } ^{\circ}\text{C}^{-1}$ inferred from observations and generally more realistic than most of
586 the models discussed in *Bellenger et al.* [2014] the differences are relatively small. However, if
587 instead we compute this parameter using the wind stresses in the NINO3.4 region, we see that it
588 increases from $2.6 \times 10^{-3} \text{ N } ^{\circ}\text{C}^{-1}$ in AREDI400 to $4.3 \times 10^{-3} \text{ N } ^{\circ}\text{C}^{-1}$ in ABERZONAL, a much
589 larger relative change. The increase in the strength of wind stress coupling is thus also
590 responsible for increasing the amplitude of ENSO as mixing increases.

591 Such significant differences are not seen, however, when linking changes in the
592 thermocline depth to wind stress (coefficient $\phi(x, \delta t)$ in equation 7). With a three or seven month
593 lag $\phi(x, 3 \text{ months}, 7 \text{ months})$ (Fig. 10b,c) shows little difference between the highest and lowest
594 mixing cases, with a shallower thermocline in the central Pacific and a deeper one in the east
595 following positive anomalies and with the amplitude and structure of the response lying very
596 close to observations in all the simulations (symbols). An enhanced response of the thermocline
597 to anomalies as the mixing increases may contribute to an increased response east of 100°W . At
598 11 months lag (Fig. 10d) there is a weak tendency for the AREDI400 run to show a stronger
599 negative anomaly around 140°W and for the ABERZONAL run to show a weaker negative
600 anomaly east of 100°W . Both of these changes would suggest that the delayed negative feedback
601 in the low mixing runs is a bit stronger than in the high mixing runs, but the differences across
602 models are much less clear than for the α and β parameters in Fig. 7.

603 Changes in ENSO amplitude due to changes in the strength of wind stress coupling have
604 previously been linked to changes in equatorial temperature gradients both across models
605 [*Anderson et al.*, 2009; *Choi et al.*, 2011] and within models [*Russell and Gnanadesikan*, 2014].
606 As shown in Table 2, this is the case for the individual models as well. On 40-year time scales,

607 the 95% confidence interval for correlating ENSO variance with other variables using 40-year
608 epochs ranges between 0.35 and 0.49 depending on the autocorrelation of the time series
609 (maximum 40 year-autocorrelation is 0.26). In general the temperature in the western basin is
610 anticorrelated with the variance at the 95% level (2nd column in Table 2). The temperature in the
611 eastern part of the basin is positively correlated with the variance (3rd column in Table 2), but not
612 always significantly at the 95% level. However, the difference between the eastern and western
613 sides of the basin shows a strong, and highly statistically significant, correlation with the
614 variance (4th column, Table 2). A scatterplot of NINO3.4 variance in the annually smoothed SST
615 vs. the SST gradient (Fig. 11) shows similar slopes across the different models. However, the
616 intercept of the line through each point cloud is clearly different, so that one cannot simply scale
617 the SST gradient in one model to compute the variance in another model. This is most likely
618 because as the mixing increases the mean state becomes more unstable (shifting the point cloud
619 up and to the left), but individual anomalies are more strongly damped (shifting the point cloud
620 down). ENSO amplitude shows a much more consistent relationship with along-equatorial
621 thermal gradient than with the amplitude of the annual cycle of SSTs (Fig. 5b).

622

623 **4. Discussion and conclusions**

624

625 In summary, as illustrated in Fig. 12, increasing A_{Redi} has a direct effect on ENSO
626 amplitude, resulting in faster damping of anomalies, but also has an indirect effect on coupling
627 that is even stronger. Some of this is because the mean state of the ocean with higher A_{Redi} is
628 more stratified and thus more responsive to changes in winds and thermocline depth, an effect

629 similar to that proposed by *Clement et al.* [1996] and found by *DiNezio et al.* [2009] for the very
630 different driver of global warming. It is also because the atmosphere that results from this mean
631 state is more sensitive to perturbations in SST, highlighting the importance of considering the
632 effects of changes in physics within fully coupled models which allow for such changes in
633 atmospheric responsiveness. The propagation of wind-driven thermocline depth anomalies,
634 however, does not change much between the models, particularly in regions where large changes
635 in SST variability are seen.

636 We have shown that the lateral mixing coefficient A_{Redi} exerts a significant control on the
637 amplitude of ENSO in a coupled climate model, but that it does so in both direct and indirect
638 ways, which act in opposite directions. Such an impact is similar to that found for chlorophyll-
639 dependent absorption in the eastern Pacific by *Anderson et al.* [2009]. In that paper it was found
640 that increasing chlorophyll sharpened the thermocline, strengthening El Nino, but cooling the
641 East Pacific in the mean, shifted the winds westward and reduced the sensitivity of the
642 atmosphere to SST anomalies. The results suggest that the large-scale temperature patterns
643 associated with changes in ENSO amplitude by *Rodgers et al.* [2004] are not merely due to
644 rectification of an asymmetric pattern, but are actually drivers of that pattern via atmospheric
645 coupling.

646 The importance of A_{Redi} raises an obvious question of how well we know this parameter.
647 There are at least three complications when thinking about this in the context of tropical
648 variability. The first is the question, noted by *Richards and Edwards* [2003], of how to account
649 for the combination of large, resolved tropical instability waves and subgridscale diffusion.
650 While tropical instability waves are found in relatively coarse models, it is far from clear that
651 these waves actually break and mix in such models. In the real world, tropical waves have been

652 found to play a major role in diffusive transport [*Jochum and Murtugudde, 2006; Abernathey*
653 *and Wortham, 2015*]. To the extent that we are “double counting” the waves by both resolving
654 and parameterizing their effects, our results will not reflect the real world. The second is the
655 question of anisotropy. Measurements [*Bauer et al., 1998*] and models [*Fox-Kemper et al., 2015*]
656 suggest that the mixing is likely to be strongly anisotropic, with larger values across the direction
657 of flow. However, it is far from clear that this diffusion actually matters dynamically, as
658 temperature and salinity gradients tend to be small along the flow direction. More work in this
659 area is needed to understand the impacts. A final question involves the vertical structure of
660 A_{Redi} . This is poorly known, as the satellite-based estimates really only capture the surface, and
661 most float experiments capture either the surface or main thermocline. Oxygen [*Gnanadesikan et*
662 *al., 2013*] suggests that values of around $1000 \text{ m}^2/\text{s}$ are most appropriate for the equatorial
663 Pacific. Our results would actually support such a lower value of mixing coefficient in our model
664 as well (though such a conclusion should be taken with caution, as it may simply reflect other
665 biases that make the ocean too responsive to the atmosphere).

666 The results of *Gnanadesikan et al.* [2013, 2015a,b] illustrate that different processes may
667 be most sensitive to mixing in different regions. With respect to El Nino, ABER2D looks a lot
668 like a model with a very high constant mixing coefficient. However, when it comes to the uptake
669 of anthropogenic carbon dioxide [*Gnanadesikan et al., 2015b*] ABER2D looks much more like
670 AREDI800 and AREDI1200, reflecting the fact that the mixing coefficient is much lower in the
671 Southern Ocean (the key region for such uptake) than in tropics. While we know the mixing
672 coefficient is not constant worldwide, studies made with models in which it is constant are still
673 critical for elucidating where lateral mixing matters for different fields and processes.

674 The close coupling (and compensation) between lateral and vertical mixing seen here also

675 highlights the importance of eddy-mixed layer interactions. The details of how the mixing
676 changes from along-isopycnal to horizontal can be quite different in different climate models,
677 with the exact threshold where the switch occurs poorly constrained [*Gnanadesikan et al.*, 2007].
678 Moreover both observations [*Moum et al.*, 2009] and models [*Holmes and Thomas*, 2015] show
679 that eddies may couple to vertical mixing. Our results suggest that much more attention may
680 need to be paid to this issue.

681 **Acknowledgements:** This work was supported under NSF grant EAR-1135382 and DOE grant
682 SC0007066. Support for RA was provided by NASA grant NNX14AI46G. We thank Nathalie
683 Burls for useful discussions and two anonymous reviewers for careful and constructive reviews.
684 The model output used in this paper is served at <http://pages.jh.edu/~agnanad1/datasets.htm>.

685 **References**

686 Abernathey, R. and Marshall, J. (2013), Global surface eddy diffusivities derived from satellite
687 altimetry, *J. Geophys. Res.-Oceans*, 118, 901–916, doi:10.1002/jgrc.20066.

688 Abernathey, R., Marshall, J., Shuckburgh, E., and Mazloff, M. (2010), Enhancement of
689 mesoscale eddy stirring at steering levels in the Southern Ocean, *J. Phys. Oceanogr.*, 40,
690 170–185, doi:10.1175/2009JPO4201..

691 Abernathey, R. P. and C. Wortham (2015), Phase speed cross spectra of eddy heat fluxes in the
692 Pacific. *J. Phys. Oceanogr.*, 45, 1285–1301, 2015, doi:10.1175/JPO-D-14-0160.1

693 Anderson, W.G., A. Gnanadesikan and A. Wittenberg (2009), Regional impacts of ocean color
694 on tropical Pacific variability, *Ocean Science*, 5,313-327, doi:10.5194/os-5-313-2009.

695 Bachman,S., B Fox-Kemper and F.C.Bryan (2015), A tracer-based inversion method for
696 diagnosing eddy-induced diffusivity and advection. *Ocean Model.*, 86, 1-15 ,
697 doi10.1016/j.ocemod.2014.11.006.

698 Bauer, S., M.S. Swenson, A. Griffa, A.J. Mariano, and K. Owens (1998), Eddy-mean flow
699 decomposition and eddy-diffusivity estimates in the tropical Pacific Ocean., 1.
700 Methodology. *J. Geophys. Res.*, 103, 30855—30871, 10.1029/1998JC900009.

701 Bellenger, H., E. Guilyardi, J. Leloup, M. Lengaigne and J. Vialard (2013), ENSO representation
702 in climate models: From CMIP3 to CMIP5, *Clim. Dynamics*, 42, 1999-2018,
703 doi:10.1007/s00382-013-1783-z.

704 Bentsen, M. and co-authors (2013), The Norwegian earth system model, NorESM1-M—Part 1:
705 description and basic evaluation of the physical climate. *Geosci. Model Dev*, **6**, 687-720,
706 doi:10.5194/gmd-6-687-2013.

707 Bunge, L. and A. Clarke (2014), On the Warm Water Volume and Its Changing Relationship
708 with ENSO. *J. Phys. Oceanogr.*, **44**, 1372–1385, doi: 10.1175/JPO-D-13-062.1.

709 Capotondi, A. (2013), ENSO diversity in the NCAR CCSM4 climate model, *J. Geophys. Res.*,
710 **118**, 4755-4770, doi:10.1002/jgrc.20335.

711 Carton, J. and B.S. Giese (2008), A reanalysis of ocean climate using the Simple Ocean Data
712 Assimilation, *Monthly Wea. Rev.*, **136**, 2999-3017, doi:10.1175/2007MWR1978.1.

713 Choi, J.S., S.I. An and S.-W. Yeh (2012), Decadal amplitude modulation of two types of ENSO
714 and its relationship with the mean state. *Climate Dyn.*, **28**, 2631–2644, doi:10.1007/s00382-
715 011-1186-y.

716 Clement, A.S., R. Seager, M. A. Cane, and S. E. Zebiak (1996), An Ocean Dynamical
717 Thermostat. *J. Climate*, **9**, 2190–2196. doi:[10.1175/1520-
718 0442\(1996\)009<2190:AODT>2.0.CO;2](https://doi.org/10.1175/1520-0442(1996)009<2190:AODT>2.0.CO;2)

719 Cobb, K.M, Westphal, N., Sayani, H.R., Watson, J.T., Di Lorenzo, E., Cheng, H., Edwards,
720 R.L., and Charles, C.D. (2013), Highly Variable El Niño–Southern Oscillation Throughout
721 the Holocene, *Science* **339**, 67-70, doi: 10.1126/science.1228246.

722 Danabasoglu, G., S. Bates, B. P. Briegleb, S. R. Jayne, M. Jochum, W. G. Large, S. Peacock, and
723 S. G. Yeager (2012), The CCSM4 Ocean Component. *J. Climate*, **25**, 1361-1389,
724 doi:10.1175/JCLI-D-11-00091.1.

725 Danabasoglu G. and J. Marshall, (2007) Effects of vertical variation of thickness diffusivity in an
726 ocean general circulation model, *Ocean Modell.*, 18, 122-141,
727 doi:10.1016/j.ocemod.2007.03.006.

728 DiNezio, P., A.C. Clement, G.A. Vecchi, B.J. Soden, B.P. Kirtman, and S. Lee, (2009) Climate
729 Response of the Equatorial Pacific to Global Warming. *J. Climate*, 22, 4873–4892, doi:
730 10.1175/2009JCLI2982.1

731 Dunne, J.P., J.G. John, A. J. Adcroft, S.M. Griffies, R.W. Hallberg, E.N. Shevliakova, R.J.
732 Stouffer, W. Cooke, K.A. Dunne, M.J. Harrison, J.P. Krasting, H. Levy, S.L. Malyshev,
733 P.C.D. Milly, P.J. Phillips, L.A. Sentman, B.L. Samuels, M.J. Spelman, M. Winton, A.T.
734 Wittenberg and N. Zadeh, (2012), GFDL's ESM2 global coupled climate-carbon Earth
735 System Models Part I: Physical formulation and baseline simulation characteristics, *J.*
736 *Climate*, 6646—6665, <http://dx.doi.org/10.1175/JCLI-D-11-00560.1>.

737 Flato, G., J. Marotzke, B. Abiodun, P. Braconnot, S.C. Chou, W. Collins, P. Cox, F. Driouech, S.
738 Emori, V. Eyring, C. Forest, P. Gleckler, E. Guilyardi, C. Jakob, V. Kattsov, C. Reason and
739 M. Rummukainen (2013), Evaluation of Climate Models. In: *Climate Change 2013: The*
740 *Physical Science Basis. Contribution of Working Group I to the Fifth Assessment Report of*
741 *the Intergovernmental Panel on Climate Change* [Stocker, T.F., D. Qin, G.-K. Plattner, M.
742 Tignor, S.K. Allen, J. Boschung, A. Nauels, Y. Xia, V. Bex and P.M. Midgley (eds.)].
743 Cambridge University Press, Cambridge, United Kingdom and New York, NY, USA.

744 Fogli, P., E. Manzini, M. Vichi, A. Alessandri, L. Patara, S. Gualdi, E. Scoccimarro, S. Masina
745 and A. Navarra (2009), INGV-CMCC Carbon (ICC): a carbon cycle earth system model,
746 Technical Rep. 61, Centro Euro-Mediterraneo per i Cambiamenti Climatici, Bologna.

747 Fox-Kemper, B., R. Ferrari and R. Hallberg (2008), Parameterization of mixed layer eddies, Part
748 I: Theory and diagnosis. *J. Phys. Oceanogr.*, 38, 1145–1165,
749 <http://dx.doi.org/10.1175/2007JPO3792.1>.

750 Galbraith, E.D., A. Gnanadesikan, J.P. Dunne and M.R. Hiscock (2010), Regional impacts of
751 iron-light colimitation in a biogeochemical model, *Biogeosciences*, 7, 1043-1064,
752 doi:10.5194/bg-7-1043-2010.

753 Galbraith, E.D., E.Y. Kwon, A. Gnanadesikan, K.B. Rodgers, S.M. Griffies, J.P. Dunne, J.L.
754 Sarmiento, D. Bianchi, J. Simeon, A. T. Wittenberg, M. J. Harrison, I. Held and R.D. Slater
755 (2011), The impact of climate variability on the distribution of radiocarbon in CM2Mc- a
756 new earth system model, *J. Climate*, 24, 4230-4254. [doi:10.1175/2011JCLI3919.1](https://doi.org/10.1175/2011JCLI3919.1)

757 Gent, P. R., and J. C. McWilliams (1990), Isopycnal mixing in ocean circulation models, *J. Phys.*
758 *Oceanogr.*, 20,150-155, [doi:10.1175/1520-0485\(1990\)020%3C0150:IMIOCM%3E2.0.CO;2](https://doi.org/10.1175/1520-0485(1990)020%3C0150:IMIOCM%3E2.0.CO;2)

759 Gent, P. R., J. Willebrand, T. J. McDougall, and J. C. McWilliams (1995), Parameterizing eddy-
760 induced tracer transports in ocean circulation models, *J. Phys. Oceanogr.*, 25, 463-474,
761 [http://dx.doi.org/10.1175/1520-0485\(1995\)025%3C0463:PEITTI%3E2.0.CO;2](http://dx.doi.org/10.1175/1520-0485(1995)025%3C0463:PEITTI%3E2.0.CO;2)

762 Gnanadesikan, A., R. Abernathey and M.A. Pradal (2015a), Exploring the isopycnal mixing and
763 helium-heat paradoxes in a suite of Earth System Models, *Ocean Science*, 11, 591-605,
764 doi:10.5194/os-11-591-2015.

765 Gnanadesikan, A., D. Bianchi and M.-A. Pradal (2013), Critical role of mesoscale eddy diffusion
766 for supplying oxygen to hypoxic ocean waters, *Geophys. Res. Lett.*,40, 5168-5174
767 doi:10.1029/2013GL057674.

768 Gnanadesikan, A., K.W. Dixon, S.M. Griffies, V. Balaji, M. Barreiro, J. A. Beesley, W.F.
769 Cooke, T.L. Delworth, R. Gerdes, M.J. Harrison, I.M. Held., W. J. Hurlin, H.C. Lee, Z.
770 Liang, G. Nong, R.C. Pacanowski, A. Rosati, J.L. Russell, M. Spelman, B. L. Samuels, Q.
771 Song, M.J. Spelman, R. J. Stouffer, C. Sweeney, G. Vecchi, M. Winton, A. Wittenberg, F.
772 Zeng, R. Zhang, and J.P. Dunne (2006), GFDL's CM2 global coupled climate models-Part
773 2: The baseline ocean simulation, *J. Climate*, 19, 675-697, [doi:10.1175/JCLI3630.1](https://doi.org/10.1175/JCLI3630.1).

774 Gnanadesikan, A., S.M. Griffies and B.L. Samuels (2007), Effects in a climate model of slope
775 tapering in neutral physics schemes, *Ocean Modelling*,. 16, 1-16,
776 [doi:10.1016/j.ocemod.2006.06.004](https://doi.org/10.1016/j.ocemod.2006.06.004).

777 Gnanadesikan, A., M.A. Pradal and R.P. Abernathy (2015b), Isopycnal mixing significantly
778 impacts ocean anthropogenic carbon uptake, *Geophys. Res. Lett.*, 42, 4249-4255,
779 [doi: 10.1002/2015GL064100](https://doi.org/10.1002/2015GL064100).

780 Graham, F.S., J.N. Brown, C. Langlais, S.J. Marsland, A.T. Wittenberg and N.J. Holbrook
781 (2014), Effectiveness of the Bjerknes Stability Index in representing ocean dynamics,
782 *Climate Dynamics*, 43, 2399-2414, [doi: 10.1007/s00382-014-2062-3](https://doi.org/10.1007/s00382-014-2062-3).

783 Guilyardi, E. (2006), El Nino mean state-seasonal cycle interactions in a multi-model ensemble,
784 *Clim. Dyn.*, 26: 329. [doi:10.1007/s00382-005-0084-6](https://doi.org/10.1007/s00382-005-0084-6).

785 Holmes, R.M., and L. N. Thomas (2015), The Modulation of Equatorial Turbulence by Tropical
786 Instability Waves in a Regional Ocean Model. *J. Phys. Oceanogr.*, 45, 1155–1173,
787 <http://dx.doi.org/10.1175/JPO-D-14-0209.1>

788 Jin, F.F., S.T. Kim and L. Bejarano (2006) A coupled-stability analysis for ENSO, *Geophys. Res.*
789 *Lett.*, 33, L23708, [doi:10.1029/2006GL027221](https://doi.org/10.1029/2006GL027221).

790 Jochum, M. and R. Murtugudde (2006), Temperature advection by tropical instability waves.
791 Journal of Physical Oceanography, 36 (4), 592–605, <http://dx.doi.org/10.1175/JPO2870.1>.

792 Kim, D., J.-S. Kug, I. S. Kang, F. F. Jin, and A. T. Wittenberg (2007), Tropical Pacific impacts
793 of convective momentum transport in the SNU coupled GCM. *Climate Dyn.*31, 213-236,
794 doi:10.1007/s00382-007-0348-4.

795 Kim, S. T., and J.-Y. Yu (2012), The two types of ENSO in CMIP5 models. *Geophys. Res. Lett.*,
796 39, L11704, doi:10.1029/2012GL052006.

797 Large, W.G., J.C. McWilliams and S.C. Doney (1994), Oceanic vertical mixing: A review and a
798 model with a nonlocal boundary layer mixing parameterization, 32, 363-403, doi:
799 10.1029/2012GL052006.

800 Lengaigne, M., G. Madec, C. Menkes and G. Alory (2003), Impact of isopycnal mixing on the
801 tropical ocean circulation, *J. Geophys. Res.*, 108, 2156-2202.
802 <http://dx.doi.org/10.1029/2002JC001704>.

803 Lengaigne, M., U. Hausmann, G. Madec, G., C. Menkes, J. Vialard, J.M Molines, Mechanisms
804 controlling warm water volume interannual variations in the equatorial Pacific: diabatic vs.
805 adiabatic processes, (2012), *Clim Dyn.*, 38: 1031-1046. doi:10.1007/s00382-011-1051-z.

806 Lumpkin, R. and P. Flament, (2001), Lagrangian eddy statistics in the central North Pacific, *J.*
807 *Mar. Sys.*, 29, 141-145, [http://dx.doi.org/10.1016/S0924-7963\(01\)00014-8](http://dx.doi.org/10.1016/S0924-7963(01)00014-8)

808 Maes, C., G. Madec, and P. Delecluse (1997), Sensitivity of an Equatorial Pacific OGCM to the
809 Lateral Diffusion. *Mon. Wea. Rev.*, 125, 958–971. doi: [http://dx.doi.org/10.1175/1520-](http://dx.doi.org/10.1175/1520-0493(1997)125<0958:SOAEPO>2.0.CO;2)
810 [0493\(1997\)125<0958:SOAEPO>2.0.CO;2](http://dx.doi.org/10.1175/1520-0493(1997)125<0958:SOAEPO>2.0.CO;2)

811 Manizza, M., C. Le Quéré, A. J. Watson, and E. T. Buitenhuis (2005), Bio-optical feedbacks
812 among phytoplankton, upper ocean physics and sea-ice in a global model, *Geophysical*
813 *Research Letters*, 32, L05603, doi:10.1029/2004GL020778.

814 Manucharyan, G. E. and A.V. Fedorov, (2014). Robust ENSO across a Wide Range of Climates.
815 *Journal of Climate*, 27(15), 5836-5850. <http://doi.org/10.1175/JCLI-D-13-00759.1>.

816 Moum, J.N, R.C. Lien, A. Perlin, J.D. Nash, M.C. Gregg and P.J. Wiles (2009), Sea surface
817 cooling at the Equator by subsurface mixing in tropical instability waves, *Nature*
818 *Geosciences*, 2, 761-765, doi:10.1038/ngeo657.

819 Neale, R.B., J.H. Richter and M. Jochum (2008) The impact of convection on ENSO: From a
820 delayed oscillator to a series of events, *Journal of Climate*, 21, 5905-5924.

821 Ollitrault, M. and A. Colin de Verdiere (2002), SOFAR floats reveal midlatitude intermediate
822 North Atlantic General Circulation. Part I A Lagrangian descriptive view, *J. Phys.*
823 *Oceanogr.*, 32, 2020–2033, [http://dx.doi.org/10.1175/1520-](http://dx.doi.org/10.1175/1520-0485(2002)032%3C2034:SFRMIN%3E2.0.CO;2)
824 [0485\(2002\)032%3C2034:SFRMIN%3E2.0.CO;2](http://dx.doi.org/10.1175/1520-0485(2002)032%3C2034:SFRMIN%3E2.0.CO;2)

825 Osborn T. R., and C. S. Cox (1972), Oceanic fine structure, *Geol. Astron. Fluid Dyn.*, 3(1), 321–
826 345.

827 Pezzi, L.P. and K.J. Richards (2003), Effects of lateral mixing on the mean state and eddy
828 activity of an equatorial ocean, *J. Geophys. Res.*,108 (C12), 3371,
829 doi:10.1029/2003JC001834.

830 Pradal, M.A. and A. Gnanadesikan (2014), How does the Redi parameter for mesoscale mixing
831 impact climate in an Earth System Model?, *J. Adv. Model. Earth Sys.*, 6,586-601,
832 doi:/10.1002/2013MS000273.

833 Redi, M.H. (1982), Ocean isopycnal mixing by coordinate rotation, *J. Phys. Oceanogr.*, 12,
834 1154-1158, [doi:10.1175/1520-0485\(1982\)012%3C1154:OIMBCR%3E2.0.CO;2](https://doi.org/10.1175/1520-0485(1982)012%3C1154:OIMBCR%3E2.0.CO;2)

835 Richards, K. J., and N. R. Edwards (2003), Lateral mixing in the equatorial Pacific: The
836 importance of inertial instability, *Geophys. Res. Lett.*, 30, 1888,
837 doi:10.1029/2003GL017768.

838 Rodgers, K.B, P. Friedrichs and M. Latif (2004), Tropical Pacific Decadal Variability and Its
839 Relation to Decadal Modulations of ENSO. *J. Climate*, 17, 3761–3774,
840 [http://dx.doi.org/10.1175/1520-0442\(2004\)017%3C3761:TPDVAI%3E2.0.CO;2](http://dx.doi.org/10.1175/1520-0442(2004)017%3C3761:TPDVAI%3E2.0.CO;2)

841 Russell, A.. and A. Gnanadesikan (2014), Understanding long-period variability in ENSO
842 amplitude, *J. Climate*, 27, 4037-4051, <http://dx.doi.org/10.1175/JCLI-D-13-00147.1>.

843 Sandweiss, D.H., J.B. Richardson, E.J. Reitz, H.B. Rollins and K.A. Maasch (1996),
844 Geoaarcheological evidence from Peru for a 5000 Years B.P. onset of El Nino, *Science*, 273,
845 1531-1533.

846 Sandweiss, D.J., K.A. Maasch, R.J. Burger, J. B. Richardson, H.B. Rollins and A. Clement,
847 (2001), Variation in Holocene El Nino frequencies: Climate records and cultural
848 consequences in Ancient Peru, *Geology* 29, 603-606, doi: 10.1130/0091-7613(2001)
849 029<0603:VIHENO>2.0.CO;2.

850 Shuckburgh, E., Jones, H., Marshall, J., and Hill, C. (2009), Robustness of effective diffusivity
851 diagnostic in oceanic flows, *J. Phys. Oceanogr.*, 39, 1993–2009,
852 [doi:10.1175/2009JPO4122.1](https://doi.org/10.1175/2009JPO4122.1).

853 Stevenson, S., B. Fox-Kemper, M. Jochum, B. Rajagopalan, and S.G. Yeager, (2010), ENSO
854 Model Validation Using Wavelet Probability Analysis. *J. Climate*, 23, 5540–5547,
855 <https://doi.org/10.1175/2010JCLI3609.1>

856 Stevenson, S., B. Fox-Kemper, M. Jochum, R. Neale, C. Deser, and G. Meehl, (2012), Will
857 There Be a Significant Change to El Niño in the Twenty-First Century? *J. Climate*, 25,
858 2129–2145. <http://dx.doi.org/10.1175/JCLI-D-11-00252.1>.

859 Stevenson, S. L. (2012), Significant changes to ENSO strength and impacts in the twenty-first
860 century: Results from CMIP5. *Geophys. Res. Lett.*, 39, L17703,
861 [doi:10.1029/2012GL052759](https://doi.org/10.1029/2012GL052759).

862 Torrence, C. and P.J. Webster (1999), Interdecadal changes in the El Niño-monsoon system, *J.*
863 *Climate*, 12, 2679-2690, [doi:10.1175/1520-0442\(1999\)012%3C2679:ICITEM%3E2.0.CO;2](https://doi.org/10.1175/1520-0442(1999)012%3C2679:ICITEM%3E2.0.CO;2)

864 Tulloch, R., R. Ferrari, O. Jahn, A. Klockner, J. LaCasce, J.R. Ledwell, J. Marshall, M. Messias,
865 K. Speer, and A. Watson, (2014) Direct Estimate of Lateral Eddy Diffusivity Upstream of
866 Drake Passage. *J. Phys. Oceanogr.*, 44, 2593–2616, doi: 10.1175/JPO-D-13-0120.1

867 van Oldenborgh, G.J., S.Y. Philip and M. Collins (2005), El Niño in a Changing Climate: A
868 multi-model study, *Ocean Science*, 1, 81–95, doi:10.5194/os-1-81-2005.

869 Visbeck, M., Marshall, J., Haine, T., and Spall, M. (1997), Specification of eddy transfer
870 coefficients in coarse-resolution ocean circulation models, *J. Phys. Oceanogr.*,27, 381–402,
871 doi:[http://dx.doi.org/10.1175/1520-0485\(1997\)027%3C0381:SOETCI%3E2.0.CO;2](http://dx.doi.org/10.1175/1520-0485(1997)027%3C0381:SOETCI%3E2.0.CO;2)10.1175
872 Zhang S., M.J. Harrison, A. Rosati, and A.T. Wittenberg, 2007: System design and evaluation of
873 coupled ensemble data assimilation for global oceanic climate studies. *Mon. Weather. Rev.*,
874 135, 3541–3564, <http://dx.doi.org/10.1175/MWR3466>.

	Amplitude of annual smoothed SST	Amplitude of annually smoothed τ_x (Pa)	Amplitude of annually smoothed Z_{20} (m)
Observations	SODA:0.71 ECDA:0.69	ECMWF: 0.0083 ECDA: 0.0062	SODA: 9.2 ECDA: 9.9
ARED1400	0.82	0.0056	6.3
ARED1800	0.83	0.0060	6.5
ARED11200	0.94	0.0067	7.1
ARED12400	1.00	0.0080	7.8
ABER2D	0.98	0.0079	8.1
ABERZONAL	1.03	0.0087	8.7

875

876 **Table 1:** RMS anomalies for the six models and observations in the NINO3.4 region (170W-
877 120W, 5S-5N). Uncertainties in amplitudes are calculated from the spread of the seven
878 individual centuries of the run. Uncertainties in the amplitude of SST variability are 0.03C, in
879 wind stress 2×10^{-4} Pa and in z_{20} 0.3m, so that differences between ARED1400 and ARED1800
880 are either insignificant or marginally significant for SST and z_{20} , but the increase in variance
881 associated with all the other simulations is likely to be significant.

882

	West Pacific 150E-160E	East Pacific 120W-110W	(150-160E) minus (120W-110W)
ARED1400	-0.74	0.07	-0.77
ARED1800	-0.73	0.61	-0.86
ARED11200	-0.89	0.22	-0.90
ARED12400	-0.80	0.16	-0.87
ABER2D	-0.71	0.28	-0.83
ABERZONAL	-0.78	0.71	-0.93

883

884 **Table 2:** Correlation between NINO3.4 variance over a 40 year time period and local SSTs
885 smoothed over 40 years. Bold values exceed the 95% confidence level for 17 degrees of
886 freedom.

887

888

889 **Figure Captions**

890 **Figure 1:** Mixing coefficients in different coupled models. (A) “Thickness” mixing coefficient
891 based on theory of *Green* [1970] and *Visbeck et al.*, [1997] in the ESM2Mc model of *Galbraith*
892 *et al.*, [2011]. (B) A_{Redi} coefficient in the NCAR CESM averaged over the top 200m of the water
893 column (distribution at 500m is very similar to Fig. 1a). (C) A_{Redi} coefficient from *Abernathey*
894 *and Marshall* [2013]. (D) Zonally averaged version of (C).

895
896 **Figure 2:** Diagnostics of the equatorial simulation in the ESM2Mc model suite. Observations are
897 shown with symbols, different simulations with different colors. (A) Mean sea surface
898 temperature between 5°S and 5°N. Uncertainties in the mean (computed by taking 40 year
899 averages) are of order 0.03 °C. (B) Sea surface temperature anomaly 5°S-5°N, relative to Pacific
900 zonal mean. (C) Depth of 20°C isotherm in m. Uncertainties in the mean values are of order
901 0.4m. (D) Zonal wind stress in Pa, uncertainties in the mean value are of order 5×10^{-4} Pa.

902
903 **Figure 3:** How changing A_{Redi} changes tropical temperatures. (A) Temperature (colors) as a
904 function of latitude and neutral density (vertical axis) at 140°W. (B) Neutral diffusive heating
905 (J_{neutral} in W/m^3 , colors) and density (contours) at 140°W, showing upward transfer of heat
906 along isopycnal surfaces. Thick blue line shows mixed layer depth. (C) Difference in heating
907 terms between AREDI2400 and AREDI400 simulation at 140°W. Colors show neutral diffusive
908 term J_{neutral} , contours show that due to implicit vertical diffusion J_{vdiff} . (D) Same as (C) but
909 averaged from 3.6°N to 3.6°S.

910

911 **Figure 4:** Measures of interannual variability in various fields between 5°S and 5°N in the model
912 suite. All data is smoothed over a year before the variance is taken. (A) SST from compared with
913 the Simple Ocean Data Assimilation 2.2.4 (SODA, *Carton and Giese, 2008*) and ECDA [*Zhang*
914 *et al., 2007*], products from 1979-2010. (B) Wind stress compared with the ERA-Interim and
915 ECDA products. (C) Depth of 20°C isotherm compared with the SODA data and ECDA
916 products. (D) Variance of the interannual SST in the NINO3.4 region smoothed over a 40-year
917 period across all the models.

918

919 **Figure 5:** Results of wavelet analysis of the NINO3.4 sea surface temperatures for the six
920 simulations (color) and Reynolds and ECDA SSTs (symbols) from 5N-5S. Complex Morlet
921 wavelets were used to compute spectral density. (A) Wavelet spectral density. (B) Relationship
922 between near-annual (0.94-1.12 yr period) variance and ENSO (1.6-8.2 yr period) band variance
923 over 40 year periods.

924

925 **Figure 6:** Regression of temperature tendency terms within NINO3.4 region (subregion from
926 3.6°S to 3.6°N) against the SST anomaly across models. Annually smoothed heating/cooling
927 terms integrated over the top 9 model levels are regressed against annually smoothed SST for the
928 last 700 years of each simulation to give coefficients with units of month⁻¹ (values of 0.1
929 correspond to heat flux sensitivities of around 15 Wm⁻²K⁻¹). Each set of bars compares these
930 regression coefficients across models (denoted by the different shading). The standard error of
931 each regression coefficient (computed by taking values for 7 independent centuries) is about 5%
932 of the mean value of each coefficient.

934 **Figure 7:** Diagnosis of coupling in the model suite. (A)-(C) show results of the multiple
935 regression in equation (1). (A) α : the coefficient linking local temperature change and z_{20} , the
936 local depth of the 20°C isotherm. Standard deviations in z_{20} are of order 7m so that 1 SD change
937 in z_{20} would produce peak changes of order 0.14 C/month. (B) β :the coefficient linking local
938 temperature change and local wind stress. Standard deviations in wind stress are of order 0.006
939 Pa, so that a 1SD change would yield changes of order 0.1C/month. (C) $1/\gamma$: the damping time in
940 months.

941
942 **Figure 8:** Breakdown of coupling coefficient by individual terms. The term balances over the
943 top 100m are broken down into temperature tendencies due to (left-hand column) advection,
944 (middle column) vertical transport at 100m and surface heat fluxes and (right-hand column)
945 lateral diffusive processes for which separate regressions are done against anomalous
946 thermocline depth (top row), wind stress (middle row) and temperature anomaly (bottom row).
947 Top row shows α ,the coefficient linking depth-averaged temperature anomaly change and local
948 20-degree isotherm depth anomaly with units of $\text{K month}^{-1} \text{ m}^{-1}$. Middle row shows β , the
949 coefficient linking depth-averaged temperature anomaly change and local wind stress in units of
950 $\text{K month}^{-1} \text{ Pa}^{-1}$. Bottom row is the damping coefficient γ , in units of month^{-1} .

951
952 **Figure 9:** Differences between ABERZONAL and AREDI400 models in the regression
953 coefficients between time tendency terms (averaged over different depths) and anomalous z_{20} (α
954 top) wind stress (β middle) and minus the temperature (γ bottom) . Black lines show the change
955 in the coefficients associated with $\left(\frac{\partial T}{\partial t}\right)_{eddy}$. Blue lines show the change in the coefficients

956 associated with $\left(\frac{\partial T}{\partial t}\right)_{vert} + \left(\frac{\partial T}{\partial t}\right)_{surf}$. Red lines show the change in the coefficients associated
957 with $\left(\frac{\partial T}{\partial t}\right)_{advect}$.

958 **Figure 10:** (A) Response of zonal wind stress to SSTs in NINO3.4 region $\mu(x)$. (B)-(D)
959 Response of thermocline depth z_{20} to wind stress changes in the NINO3.4 region $\phi(x,T)$ where T
960 denotes a lag in months.. Note that the standard deviation of the wind stress is around 0.007 Pa,
961 so that a -1000m/Pa sensitivity means that thermocline depth change from a one standard
962 deviation change are of order 10m. (B) with z_{20} lagging winds by three months. (C) with z_{20}
963 lagging winds by seven months. (D) with z_{20} lagging winds by eleven months.

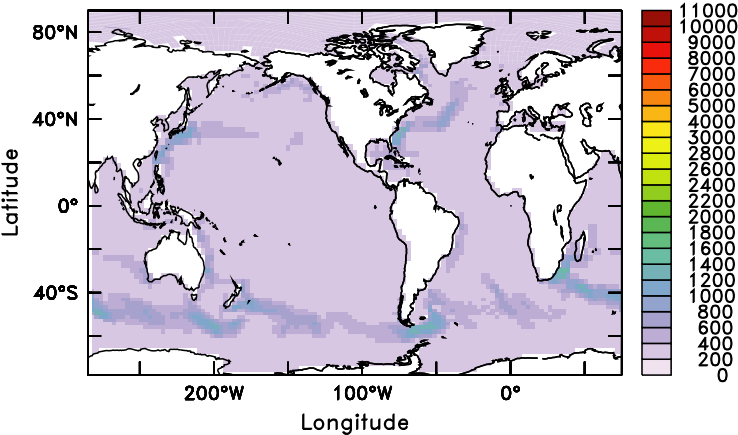
964

965 **Figure 11:** NINO3.4 SST variance vs. equatorial Pacific temperature gradients during
966 overlapping 40 year intervals (every 5 years from year 300 to 1000 is shown). SST variance
967 computed by taking the variance of annually smoothed temperatures relative to 40 year mean
968 over 40 year intervals. SST gradient is annual average over that interval.

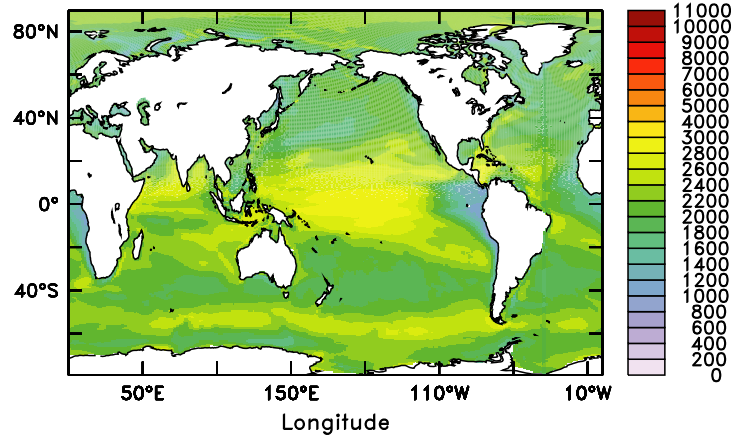
969

970 **Figure 12:** Schematic of the feedbacks involved in ENSO, and how these change as A_{Redi}
971 increases. Lines with arrows show positive feedbacks. Dashed lines terminated by circles show
972 negative feedbacks. Thickness of lines qualitatively emphasizes most important pathways
973 outlined in this paper. Increase of α is shown in Fig. 7a and linked to advection in Figs. 9a,b.
974 Increase of β is shown in Fig. 7b and linked to advection in Figs. 9c,d. Compensating changes in
975 γ are shown in Figs. 6 and 9e,f. Increase in μ is shown in Fig. 10a. Lack of change in ϕ is shown
976 in Figs. 10b-d.

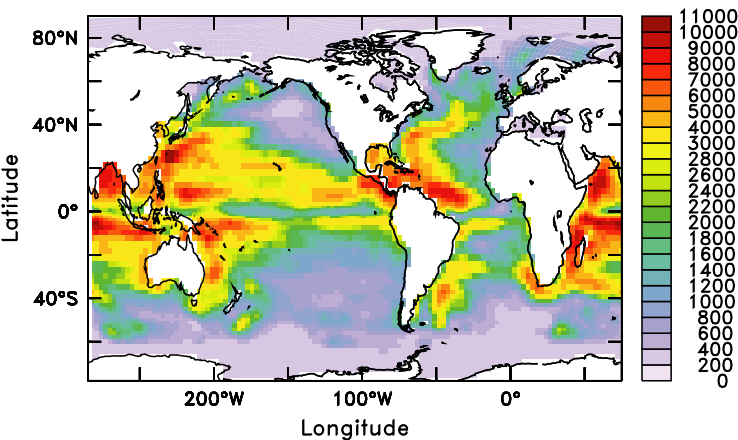
Figure 1.



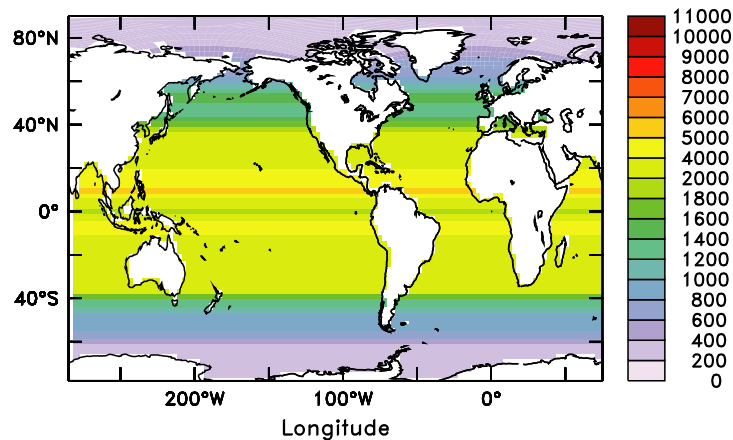
(A) A_{GM} , GFDL ESM2Mc



(B) ($A_{GM}=A_{Redi}$), 0–15m, NCAR CESM

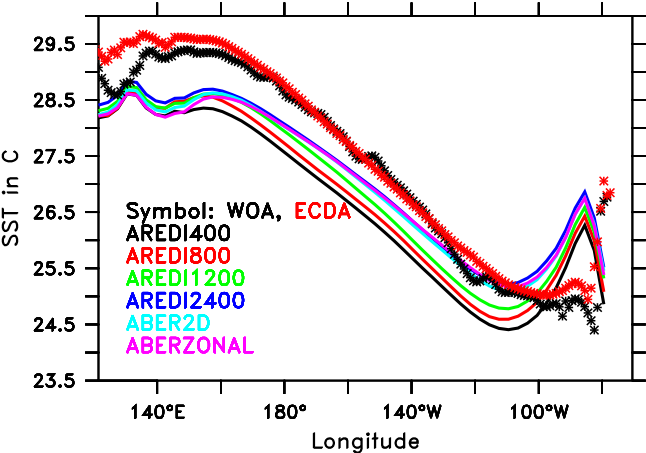


(C) A_{Redi} : ABER2D

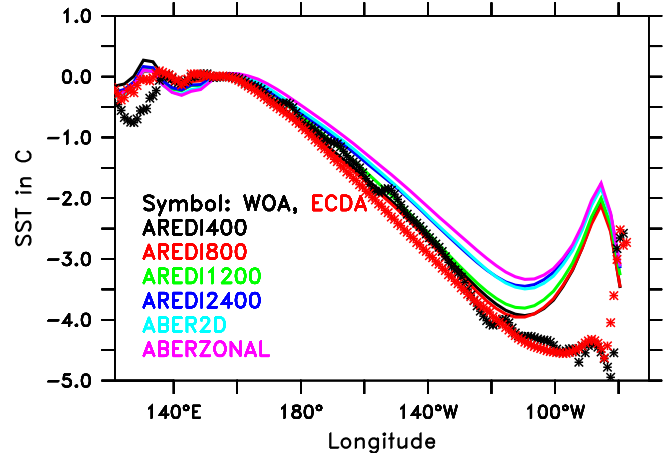


(D) A_{Redi} : ABERZONAL

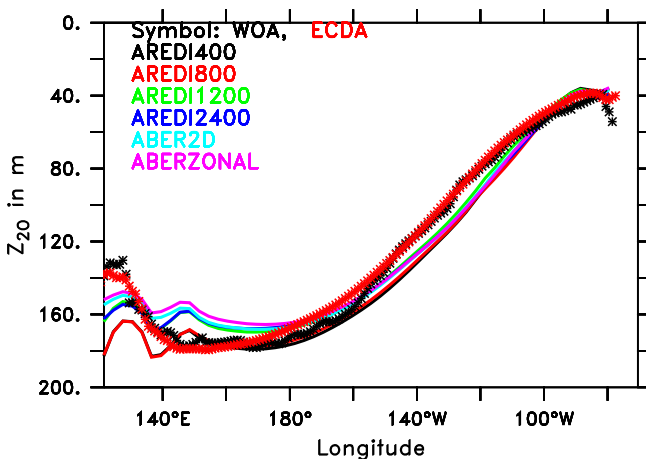
Figure 2.



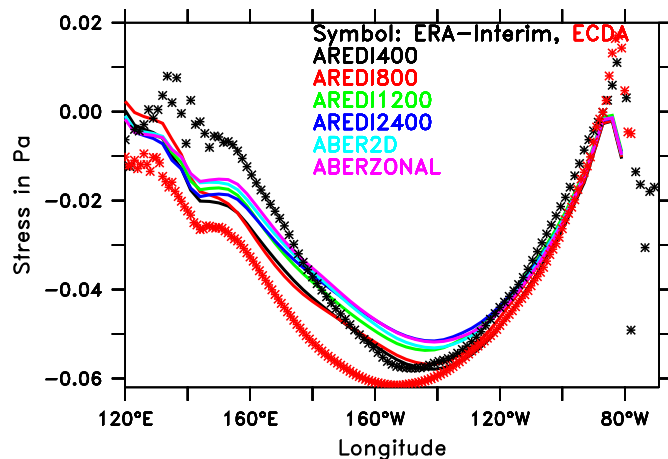
(A) SST, 5S-5N



(B) SST - SST_{WPool}, 5S-5N

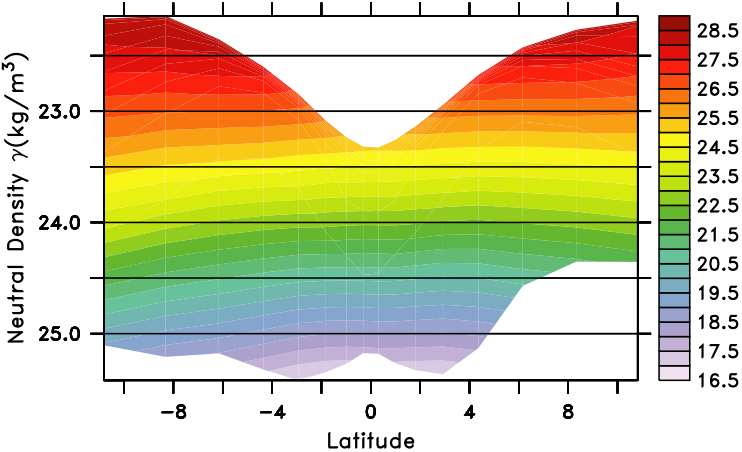


(C) Z₂₀, 5S-5N

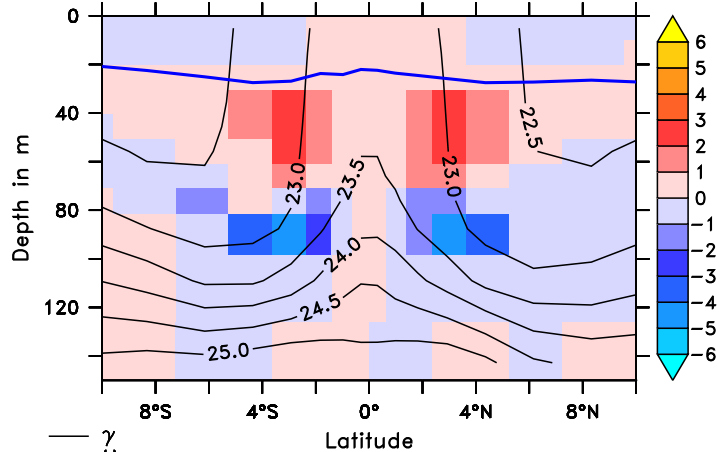


(D) Zonal wind stress, 5S-5N

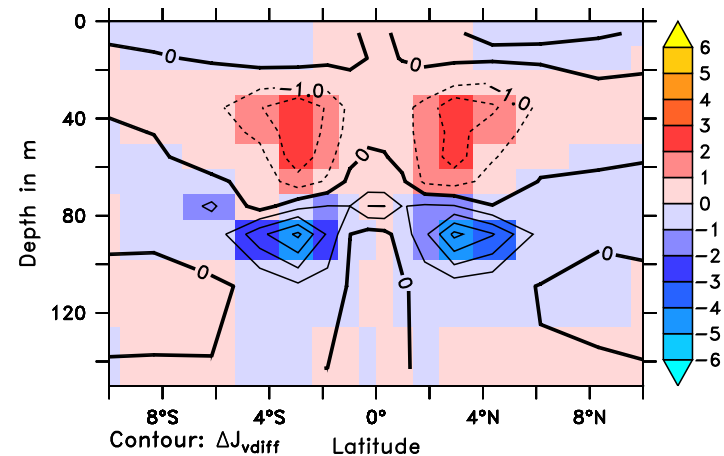
Figure 3.



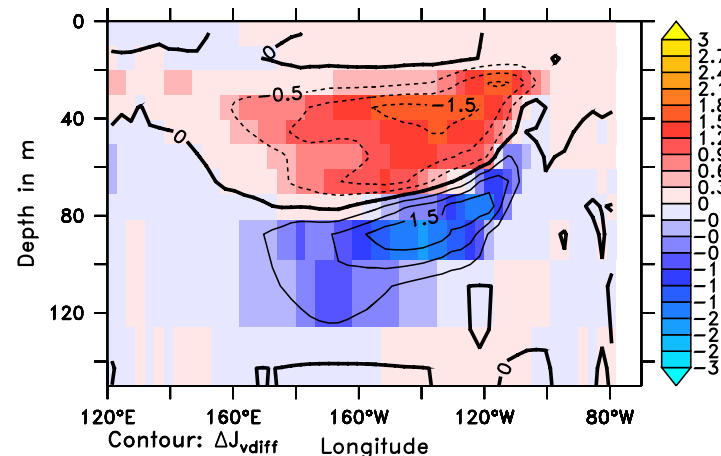
(A) Temp AREDI2400



(B) J_{neutral} (W/m^3 , AREDI2400)

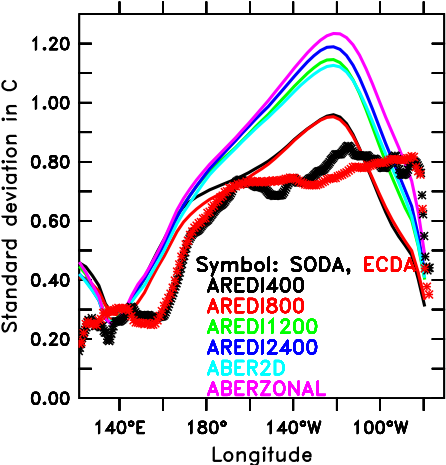


(C) $\Delta J_{\text{neutral}}$ (W/m^3 , AREDI2400-AREDI400)

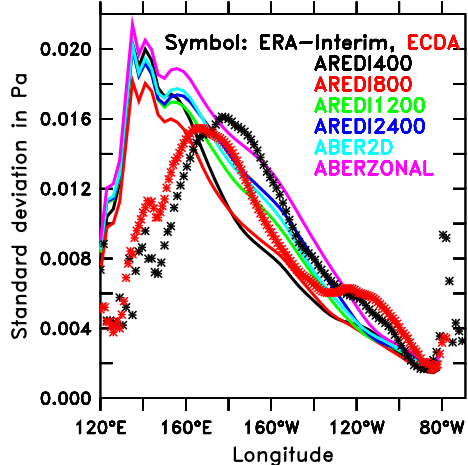


(D) $\Delta J_{\text{neutral}}$ (W/m^3 , AREDI2400-AREDI400)

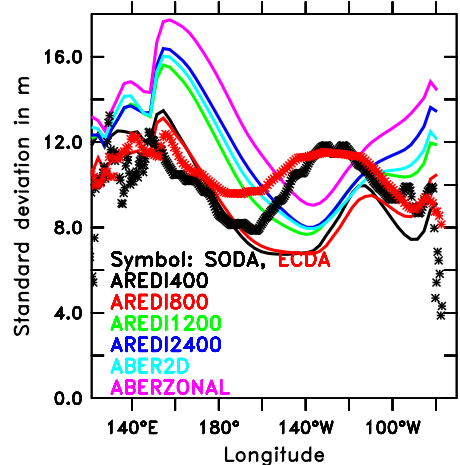
Figure 4.



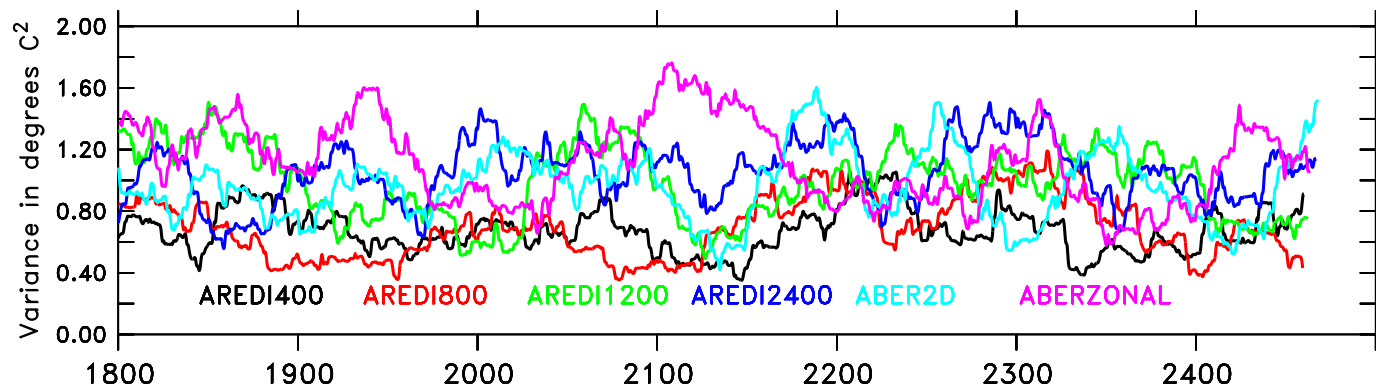
(A) SST IAV



(B) τ_x IAV



(C) Z_{20} IAV



(D) Time series of NINO3.4 Variance (1–40yr)

Figure 5.

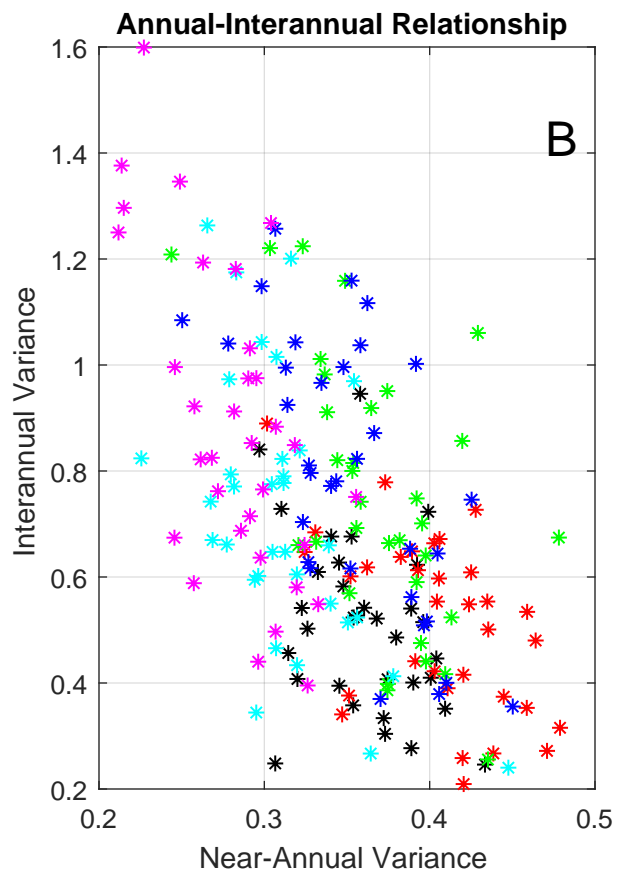
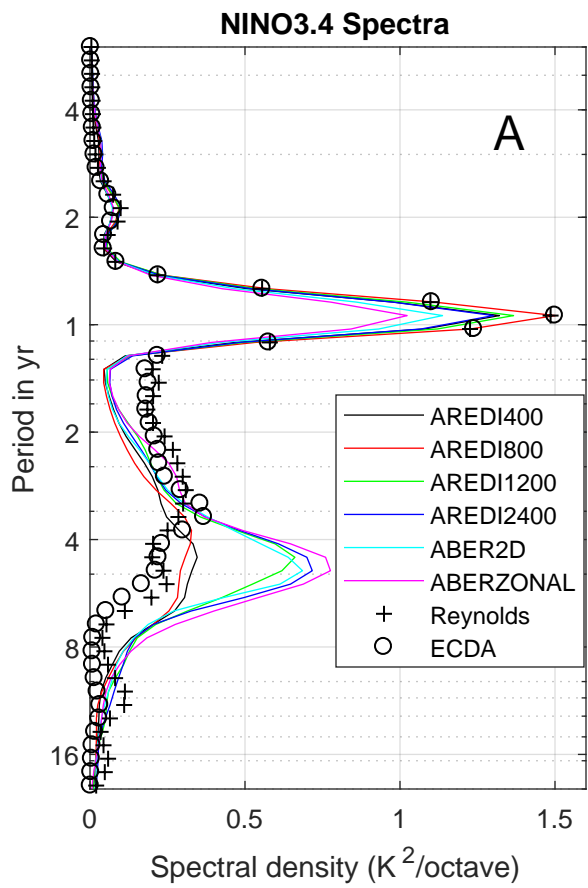


Figure 6.

NINO3.4 Regression coefficients for temperature tendencies vs. anomalies

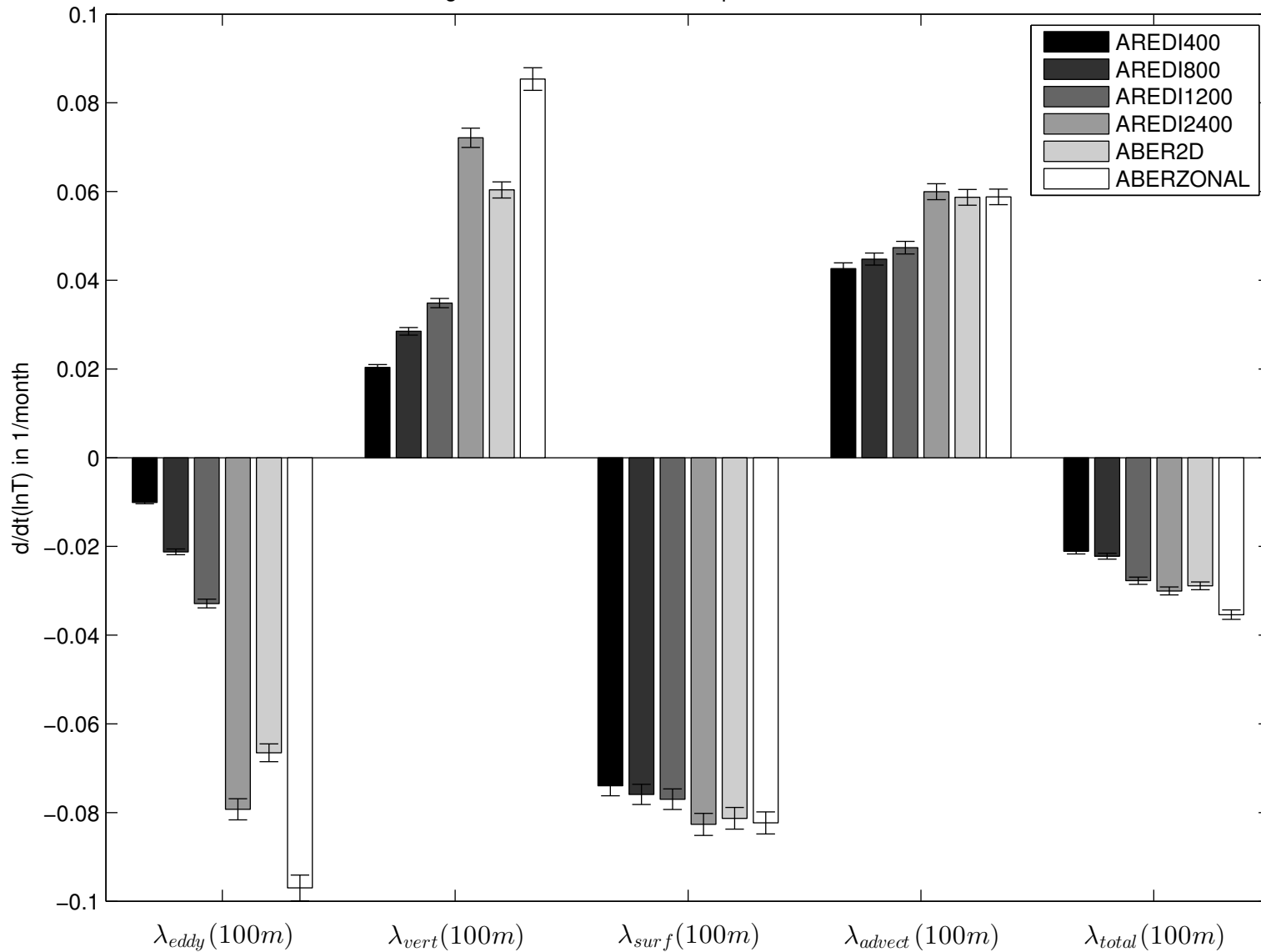


Figure 7.

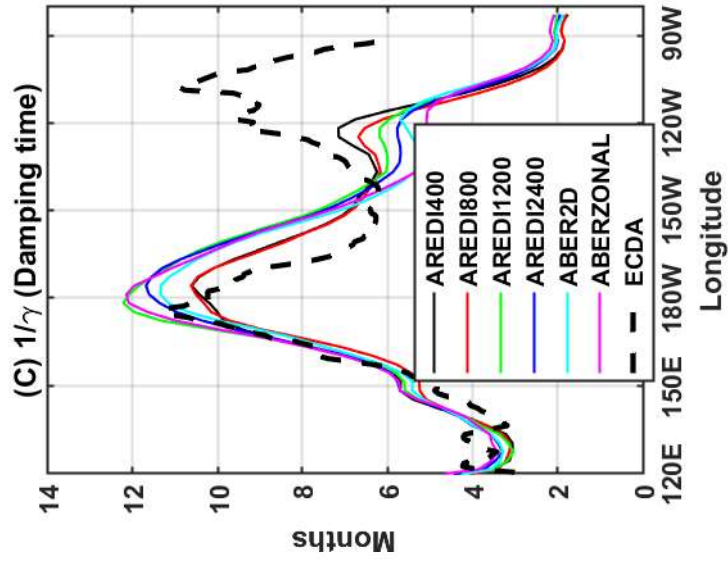
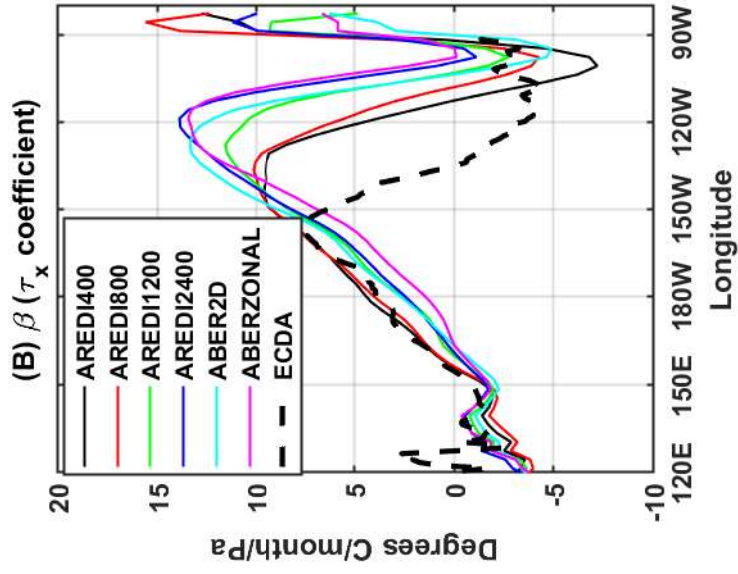
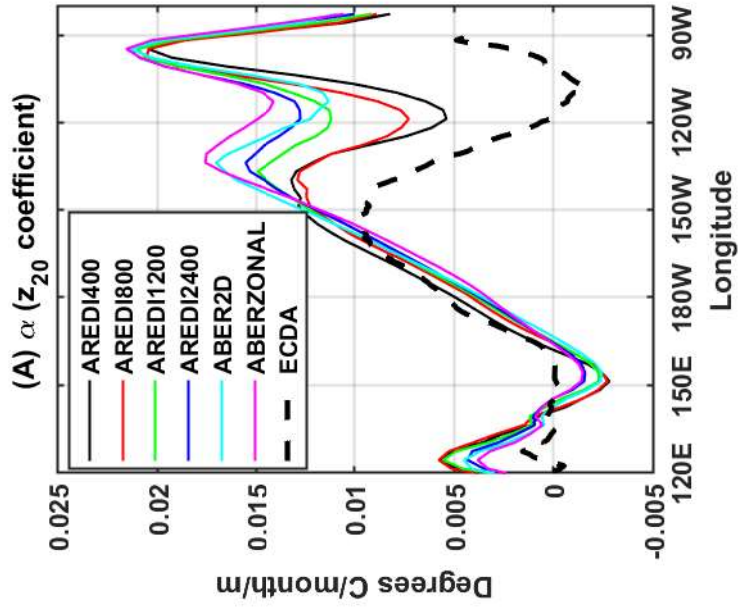


Figure 8.

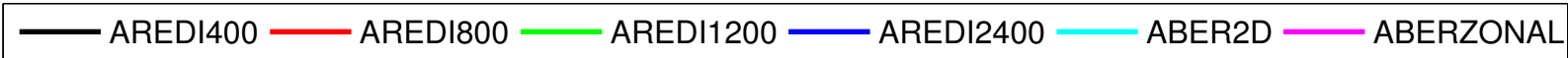
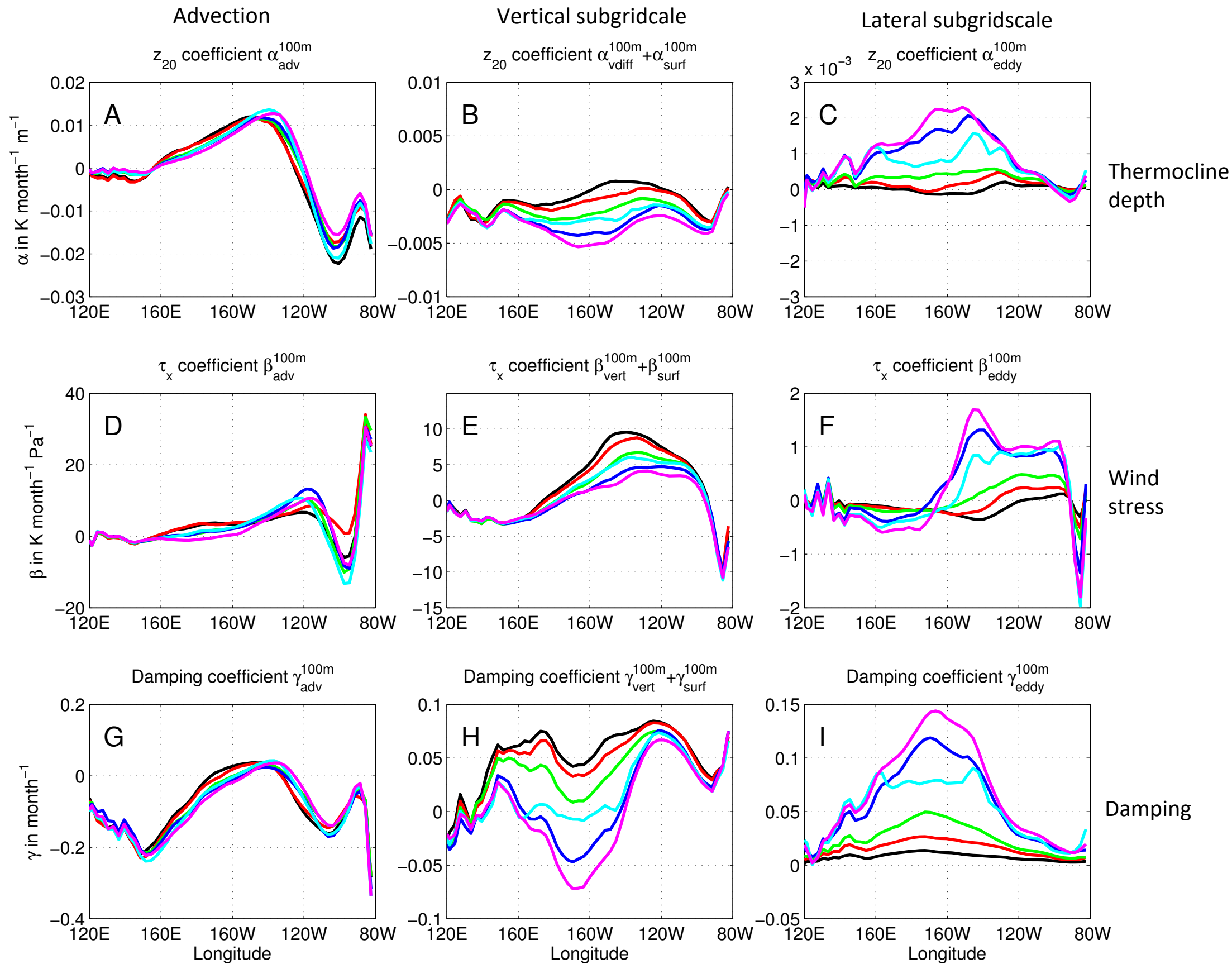


Figure 9.

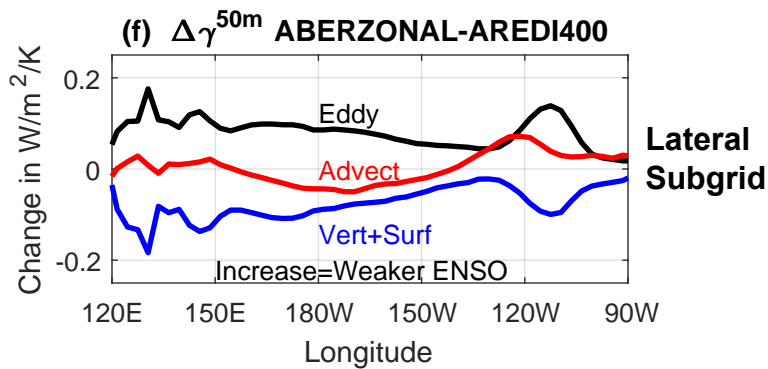
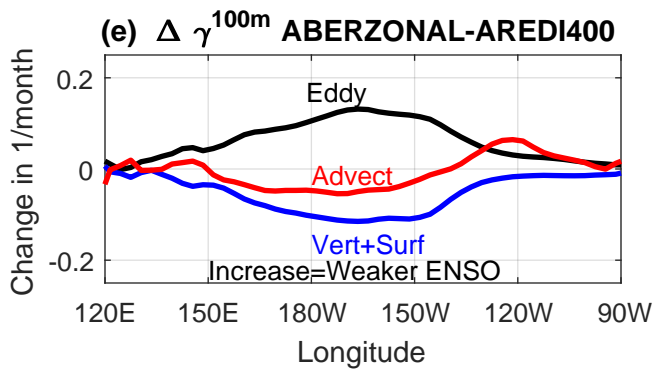
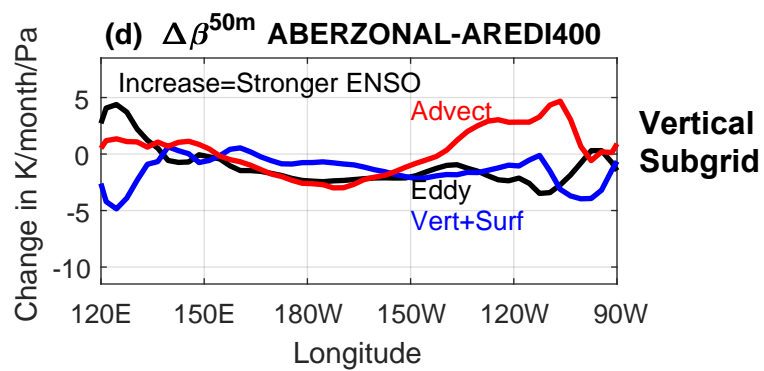
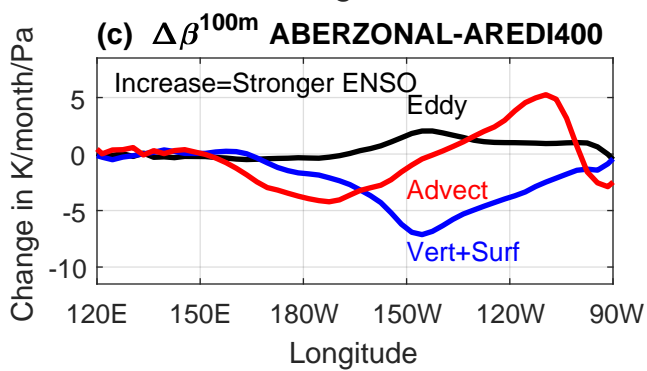
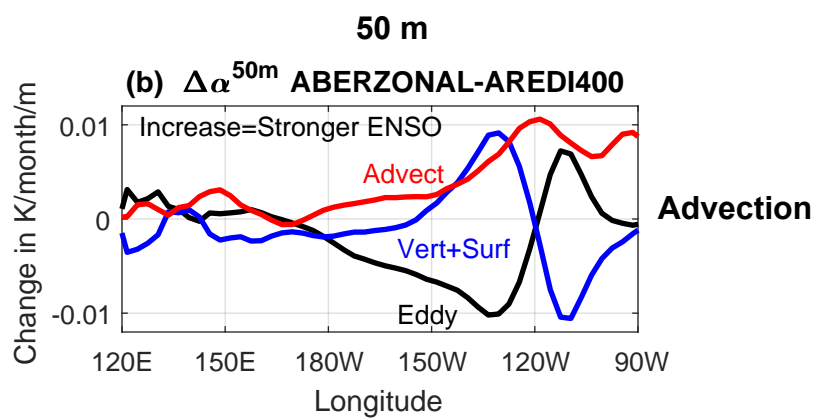
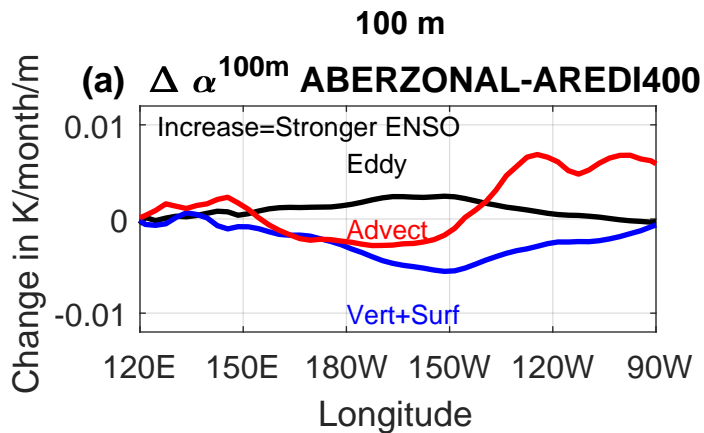
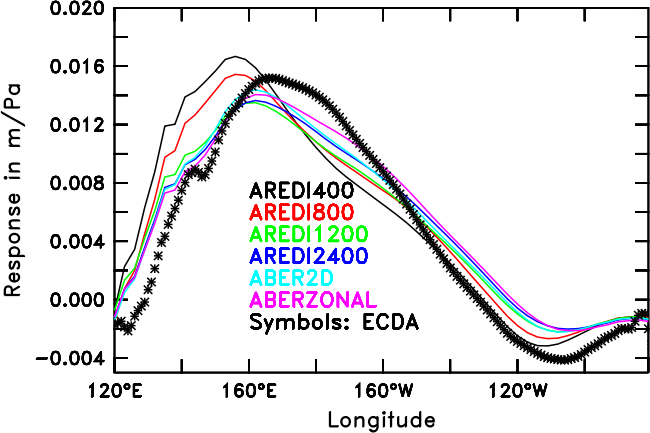
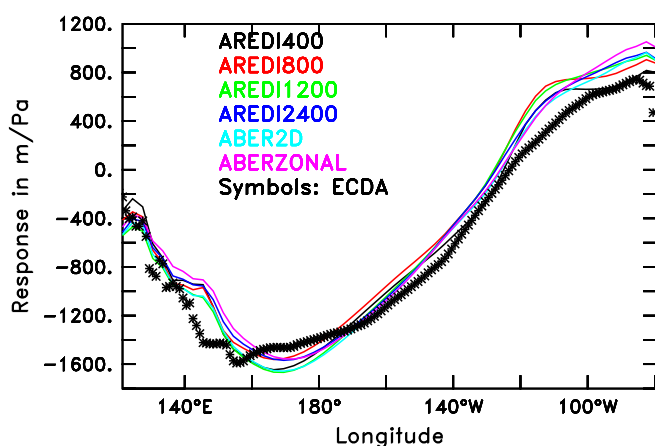


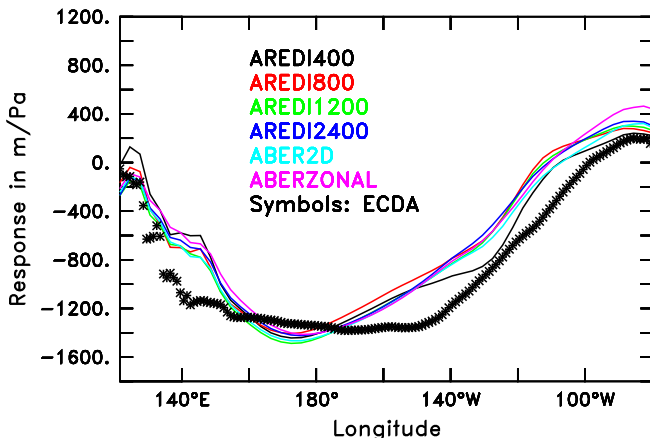
Figure 10.



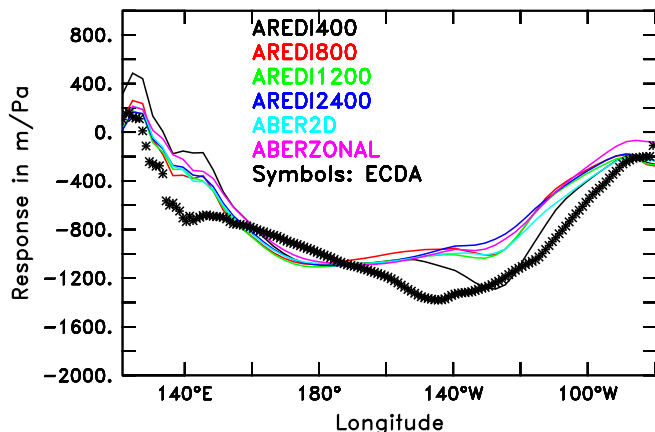
(A) $\mu:\tau_x$ response to NINO3.4 SST



(B) $\phi(3):Z_{20}$ response to NINO3.4 τ_x , 3 mo. lag

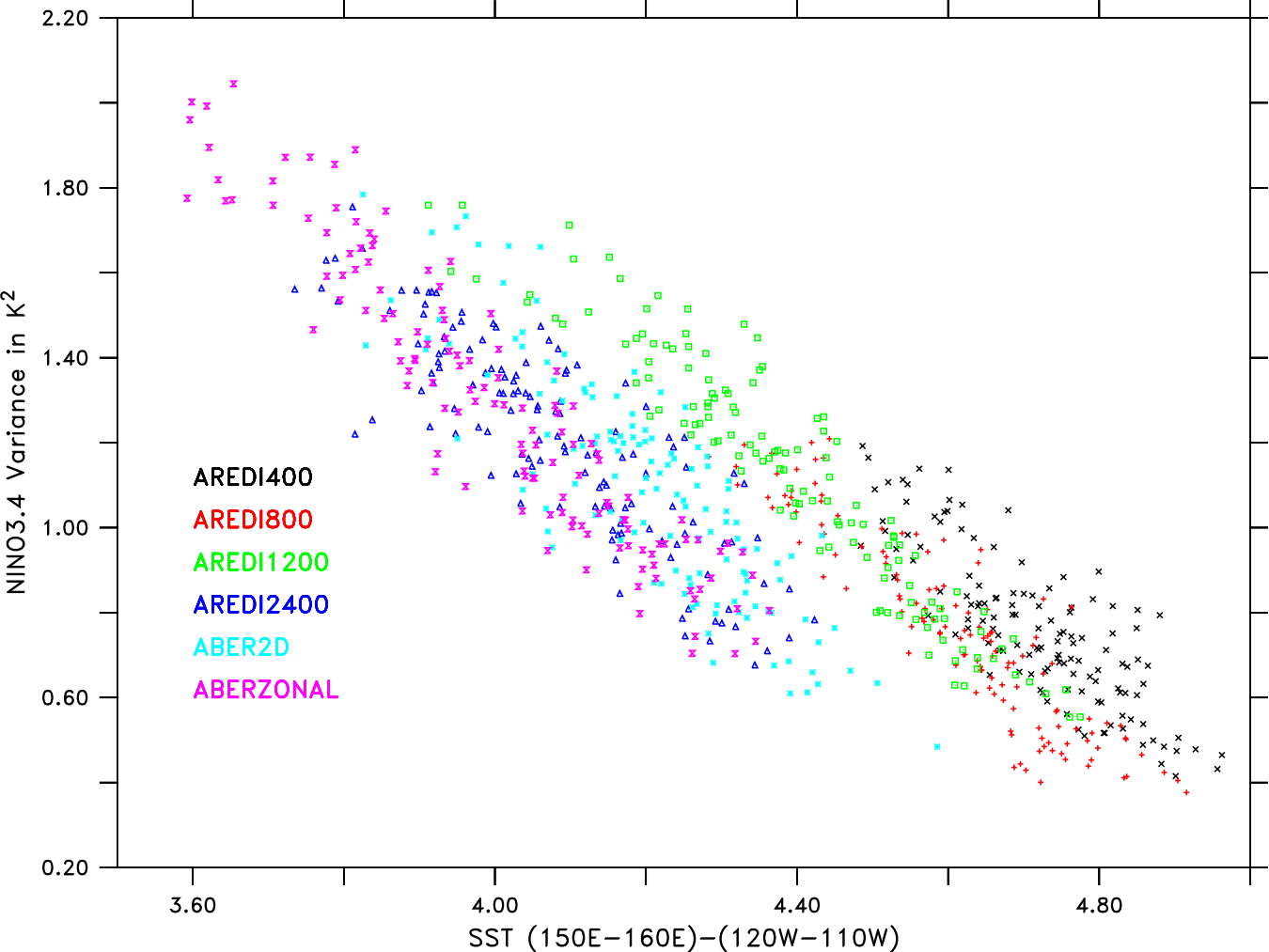


(C) $\phi(7):Z_{20}$ response to NINO3.4 τ_x , 7 mo. lag



(D) $\phi(11):Z_{20}$ response to NINO3.4 τ_x , 11 mo. lag

Figure 11.



SST Gradient and NINO3.4 Variance

Figure 12.

